Earth and Planetary Science Letters 335–336 (2012) 121–134

Contents lists available at SciVerse ScienceDirect

Earth and Planetary Science Letters

journal homepage: www.elsevier.com/locate/epsl

Environmental changes across the Triassic–Jurassic boundary and coeval volcanism inferred from elemental geochemistry and mineralogy in the Kendlbachgraben section (Northern Calcareous Alps, Austria)

József Pálfy [a,b,*], Norbert Zajzon [c]

[a] Department of Physical and Applied Geology, Eötvös Loránd University, Pázmány P. sétány 1/C, Budapest H-1117, Hungary
[b] Research Group for Paleontology, Hungarian Academy of Sciences – Hungarian Natural History Museum – Eötvös Loránd University, POB 137, Budapest H-1431, Hungary
[c] Institute of Mineralogy and Geology, University of Miskolc, Miskolc-Egyetemváros H-3515, Hungary

ARTICLE INFO

Article history:
Received 30 September 2011
Received in revised form
17 January 2012
Accepted 25 April 2012
Editor: P. DeMenocal
Available online 15 June 2012

Keywords:
Triassic–Jurassic boundary
end-Triassic extinction
Northern Calcareous Alps
micromineralogy
rare earth elements
redox-sensitive elements

ABSTRACT

The end-Triassic extinction (ETE), one of the five largest Phanerozoic mass extinctions, is associated with rapid and severe environmental change, but existing data permit alternative models of causation. Volcanism in the Central Atlantic Magmatic Province (CAMP) has been proposed as the main trigger, but direct evidence for this linkage is scarce. To help constrain scenarios for the ETE and other Triassic–Jurassic boundary (TJB) events, we obtained a temporally highly resolved, multidisciplinary dataset from the Kendlbachgraben section in the Northern Calcareous Alps in Austria. The section belongs to the same paleogeographic unit (Eiberg Basin) and share similar stratigraphy with the recently selected base Jurassic Global Stratotype Section and Point at Kuhjoch.

Micromineralogic study of the topmost bed of the Rhaetian Kössen Formation revealed pseudomorphs of altered, euhedral pyroxene and amphibole crystals. Their well-faceted morphology is consistent with their origin from distal mafic volcanic ash fallout. Spherical grains were also observed in the same bed, likely representing clay-altered volcanic glass. Clay minerals of this bed include low- to medium-charged smectite and Mg-vermiculite, both typical alteration products of mafic rocks. The same bed yielded a rare earth element pattern that differs from all other levels in an enrichment of heavy REEs, hinting at some minor contribution from mafic magmatic material. These features from a layer that was deposited very near to the TJB are interpreted as direct evidence of CAMP volcanism, coeval or immediately preceding the ETE and the initial negative carbon isotope anomaly.

The kaolinite-dominated clay mineral spectrum of the overlying boundary mudstone records intensive weathering under hot and humid greenhouse conditions. Redox-sensitive minor and trace elements do not support the development of widespread anoxia in the studied section. Although pyrite is common in several layers, framboid size indicates formation within a reductive zone, below the sediment/water interface, rather than in an anoxic water column.

Our data provide a direct link between uppermost Triassic marine strata and CAMP-derived material. They support scenarios where CAMP volcanism induced climate and other environmental change, which in turn triggered the ETE and that is also reflected in the carbon isotope anomalies.

1. Introduction

The Triassic–Jurassic boundary (TJB) is preceded by one of the five largest Phanerozoic biotic crises, the end-Triassic extinction (ETE) (Alroy, 2008; Raup and Sepkoski, 1982), which in turn was associated with and likely triggered by rapid and severe environmental change (Hesselbo et al., 2007). The biotic change is manifest in a pronounced loss of global diversity (Sepkoski, 1981, 1993), major turnover in several marine and terrestrial groups (Carter and Hori, 2005; Flügel, 2002; Kiessling et al., 2007; McElwain and Punyasena, 2007; Olsen et al., 1987) and ecologic reorganization (McElwain et al., 2007; McGhee et al., 2004). A major perturbation of the global carbon cycle likely reflects environmental disturbances and is recorded by carbon isotope anomalies in the TJB interval, documented at numerous localities worldwide (Galli et al., 2007; Guex et al., 2004; Hesselbo et al., 2002; Pálfy et al., 2001; Ruhl et al., 2009; Ward et al., 2001). Volcanism in the Central Atlantic Magmatic Province (CAMP) has

* Corresponding author at: Department of Physical and Applied Geology, Eötvös Loránd University, Pázmány P. sétány 1/C, Budapest, H-1117, Hungary.
Tel.: +36 1 372 2500x8728; fax: +36 1 381 2130.
E-mail addresses: palfy@nhmus.hu (J. Pálfy), nzajzon@uni-miskolc.hu (N. Zajzon).

0012-821X/$ - see front matter © 2012 Elsevier B.V. All rights reserved.
http://dx.doi.org/10.1016/j.epsl.2012.01.039

been proposed to be synchronous with and therefore considered as the trigger for concomitant environmental and biotic change (Marzoli et al., 1999, 2004; Pálfy, 2003). The ETE and TJB events have been in the focus of much recent research effort, yet several questions about the trajectory and causal chain of events remain open to debate (Hesselbo et al., 2007). Significantly, the key role of CAMP volcanism in triggering the extinction has been doubted (Whiteside et al., 2007) and alternative scenarios invoking a putative extraterrestrial impact event (Olsen et al., 2002), rapid sea level changes (Hallam and Wignall, 1999) or widespread marine anoxia (Hallam, 1995) have been proposed. Other possible proximate causes of the extinction include climate change, notably extreme greenhouse warming (McElwain et al., 1999; Schaller et al. 2011; Steinthorsdottir et al., 2011) and a marine biocalcification crisis (Hautmann, 2004; Hautmann et al., 2008). To further test these competing models of the TJB events, we obtained a temporally highly resolved, multidisciplinary dataset from the Kendlbachgraben section in Austria.

The Northern Calcareous Alps is a classical area of TJB studies and the section at Kendlbachgraben is the one with longest history of research (Golebiowski and Braunstein, 1988; Hallam, 1990; Suess and Mojsisovics, 1868). The search for a Global Stratotype Section and Point (GSSP) for the system boundary generated much renewed interest in the TJB in general, and in the Austrian sections in particular. The newly selected base Jurassic GSSP at Kuhjoch (Hillebrandt et al., 2007) and the Kendlbachgraben section are both located within the Eiberg Basin (Fig. 1), now separated by 130 km, and share similar stratigraphies. Thus our results reported herein have both regional and global relevance in constraining models for the ETE and TJB events.

The Kendlbachgraben section preserves a marine succession across the TJB which, together with the other well-correlated sections in the Eiberg Basin (Fig. 2), provide an excellent record of both the biotic turnover in various fossil groups and the significant changes in sedimentation (Golebiowski, 1990; Krystyn et al., 2005). The evolution of carbon isotope composition yielded a useful proxy record of environmental change (Ruhl et al., 2009).

Here we further explore the geochemistry and mineralogy of this section, in order to answer some of the remaining questions about the ETE and TJB events. Key issues addressed in this contribution concern climate change around the TJB in the source area of terrigenous sediment input, the redox conditions of local sedimentary environments, and detection of any volcanically derived material in the section that might allow direct correlation with CAMP volcanic activity. Changes in humidity are inferred from major element chemistry reflecting detrital input, variations in clay mineralogy and enrichment in immature terrigenous components. Development of oxygen deficient conditions is tracked on the basis of redox-sensitive trace elements and distribution of pyrite. Clues of contemporaneous volcanism are sought in the rare earth elements (REE) abundance patterns and the micromineralogical spectrum.

2. Geological setting

The Kendlbachgraben section is located about 30 km southeast of Salzburg and 8 km southwest of Wolfgangsee in the Osterhorn Range in Salzkammergut, Austria. Access is via a forest road in the Zinkenbach valley. The studied section is exposed on the steep hillside immediately above the forest road (coordinates 47° 41' 21"N, 13° 21' 37"E), only ~300 m NW from the point where the road crosses the gully which exposes the classical, long-known Kendlbachgraben section. The stratigraphic significance of this locality for the Triassic–Jurassic boundary was first recognized by Suess and Mojsisovics (1868). Modern studies focussed on palynostratigraphy (Morbey, 1975), changes in facies and macrofauna (Golebiowski and Braunstein, 1988; Golebiowski, 1990), and carbon isotope stratigraphy (Hallam and Goodfellow, 1990; Morante and Hallam, 1996; Ruhl et al., 2009).

The Kendlbachgraben section is located within the Eiberg Basin, an elongated, Late Triassic–Early Jurassic intraplatform basin on the shelf of the western Neotethys. Correlative, stratigraphically closely similar, and well studied sections elsewhere in the presently east–west trending, 200 km long and 20 km wide Eiberg Basin include the nearby Tiefengraben (Kürschner et al., 2007), the base Jurassic GSSP at Kuhjoch (Fig. 2) and its sister section at Hochalplgraben (Hillebrandt et al., 2007; Hillebrandt and Krystyn, 2009; Bonis et al., 2009). The Kendlbachgraben section is situated in the eastern segment of the Eiberg Basin, structurally within the Osterhorn syncline, which in turn belongs to the Stauffen–Höllengebirge nappe of the northern Tirolicum unit of the Northern Calcareous Alps (Linzer et al., 1995). The Kuhjoch GSSP locality is located in the western Eiberg basin, now preserved within the Karwendel syncline. Both sections are thought to represent proximal basin facies, sandwiched between the extensive Dachstein platform and its platform margin reefs (preserved as the "Oberrhätkalk") (Krystyn et al., 2005).

At Kendlbachgraben, the base of the section is represented by the uppermost Triassic Eiberg Member of the Kössen Formation, a dark colored, pure limestone of bioclastic wackestone texture. Our XRD measurements reveal a 98–99% calcite content, and only the remaining 1–2% is of detrital and organic origin. The topmost Rhaetian conodont *Misikella posthernsteini* is reported from the highest limestone bed (Golebiowski and Braunstein, 1988).

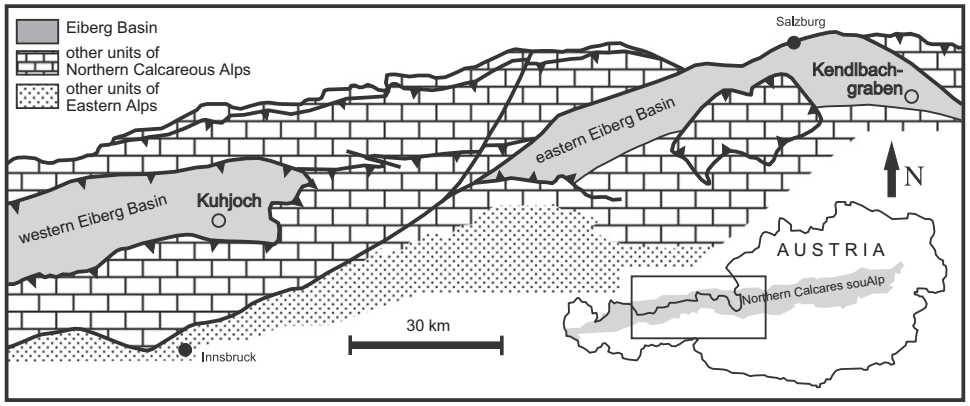

Fig. 1. Location of Triassic–Jurassic boundary sections at Kendlbachgraben (subject of this study) and Kuhjoch (Global Stratotype Section and Point, GSSP) within the Eiberg basin, shown on a schematic tectonic map of the Northern Calcareous Alps (modified from Hillebrandt and Krystyn (2009)).

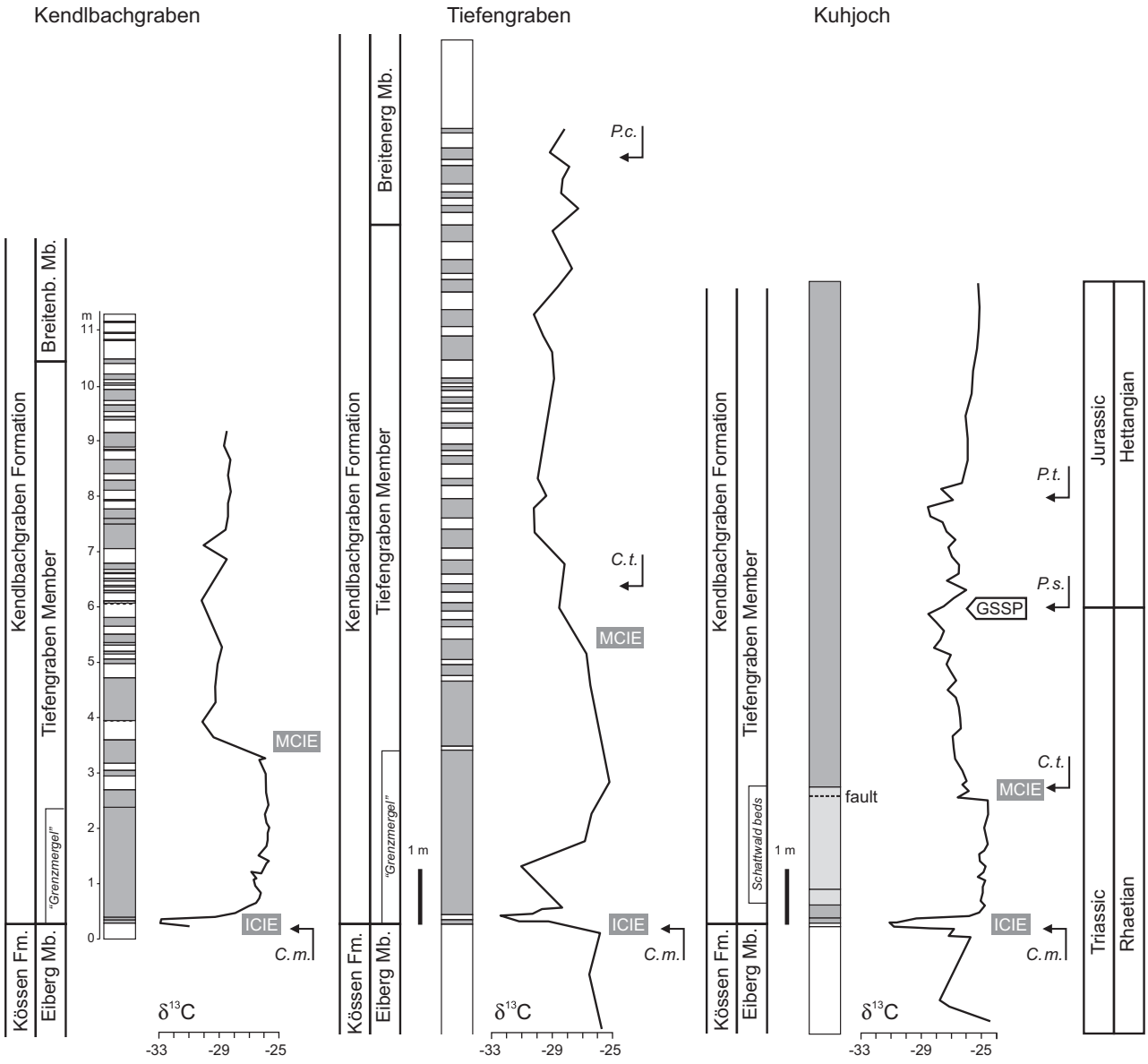

Fig. 2. Stratigraphic correlation of the Kendlbachgraben section with the basal Jurassic GSSP at Kuhjoch and the Tiefengraben sections (based on data in Hillebrandt et al. (2007), Kürschner et al. (2007) and Ruhl et al. (2009)). The simplified lithologic logs are drawn to the same scale; white denotes limestone and calcareous marl, dark gray denotes claystone and clayey marl, including the boundary mudstone. Reddish claystone of the Schattwals beds are marked by light gray. GSSP marks the officially agreed upon level of the Triassic–Jurassic boundary in the stratotype section. ICIE: Initial carbon isotope excursion. MCIE: Beginning of the main carbon isotope excursion. Lines with arrowhead mark the first and last occurrence datum of diagnostic taxa. *C. m.*: *Choristoceras marshi*; *C. t.*: *Cerebropollenites thiergartii*; *P. s.*: *Psiloceras spelae*; *P. t.*: *Psiloceras tilmanni*.

The transition at the formation boundary is represented by a 5 cm thick marlstone layer, overlain by 5 cm of brown claystone, yielding bivalves (e.g. *Cardinia*, *Chlamys*) (Golebiowski and Braunstein, 1988) and fish scales. The initial negative carbon isotope anomaly was detected at this level (Ruhl et al., 2009). The basal part of the overlying Kendlbach Formation is the ~2.5 m thick clay-rich boundary mudstone ("Grenzmergel" in the traditional terminology) which forms the basal part of the Tiefengraben Member. Early claims of a broad negative carbon isotope anomaly in this unit (Hallam and Goodfellow, 1990) were withdrawn on the basis of diagenetic overprint (Morante and Hallam, 1996). Higher upsection the Tiefengraben Member is composed of intercalated beds of marl and impure limestone, in turn overlain by the carbonate-dominated Breitenberg Member. Stable carbon isotope stratigraphy, in agreement with lithostratigraphy, permits good correlation with the GSSP section at Kuhjoch and suggests placement of the TJB in the middle of the Tiefengraben Member, where the main negative carbon isotope anomaly starts at ~3 m above the formation boundary (Ruhl et al., 2009).

3. Material and methods

A suite of 59 samples was collected from the section for whole rock major and trace element analyses. The topmost layer of the Kössen Formation was sampled in duplicate (KBL-0 and KB-1) at different times and analyzed in different batches. Samples KB-2 and KB-3 originate from the first two layers immediately overlying the Kössen Formation, whereas 11 closely spaced samples represent the "Grenzmergel", the boundary mudstone. One sample was taken from each of the 5–40 cm thick individual layers of the overlying 9.5 m of alternating shale-marlstone and limestone

lithologies of the Kendlbach Formation, except for the thickest (80 cm) marlstone interlayer which provided samples KB-31 and KB-32. From this part of the section, a total of 30 samples are from limestone beds (sample numbers prefixed KBL), whereas 28 samples are from shale or marlstone (prefixed KB). A subset of selected samples was further subjected to mineralogical analyses.

Chemical analyses were carried out at the Acme Analytical Laboratories Ltd., Vancouver, Canada. Total abundance of major oxides and several minor elements (Si, Al, Fe, Ca, Mg, Na, K, Mn, Ti, P, Cr) is reported on the basis of 0.2 g samples analyzed by inductively coupled plasma optical emission spectrometry (ICP-OES) following a lithium-metaborate/tetraborate fusion and dilute nitric acid digestion. Loss on ignition (LOI) was determined by weight difference after ignition at 1000 °C. Total carbon and sulphur analysis were done on a Leco instrument. Rare earth (La, Ce, Pr, Nd, Sm, Eu, Gd, Tb, Dy, Ho, Er, Tm, Yb, Lu) and refractory elements (Ba, Be, Co, Cs, Gd, Hf, Nb, Rb, Sc, Sn, Sr, Ta, Th, U, V, W, Y, Zr) were determined by inductively coupled plasma mass spectrometry (ICP-MS) following lithium-metaborate/tetraborate fusion and nitric acid digestion of a 0.2 g sample (using the same decomposition as for major oxides). In addition, a separate 0.5 g split was digested in aqua-regia and analyzed by ICP-MS to report the precious (Ag, Au, Cu) and base metals (As, Bi, Cd, Hg, Mo, Ni, Pb, Sb, Se, Tl, Zn).

From the analyzed elements the following were under the detection limit (given in parentheses): Ag (0.1 ppm), Au (0.5 ppb), Hg (0.1 ppm), Se (0.5 ppm) and Tl (0.1 ppm). Concentrations of Be (1 ppm), Bi (0.1 ppm), Cd (0.1 ppm), Mn (100 ppm) and Sn (1 ppm) were near their detection limit.

REE were normalized to the C1 chondrite (Anders and Grevesse, 1989). The cerium anomaly was quantified using the following equation: $Ce/Ce^{*}=Ce_N/(La_N \cdot Pr_N)^{0.5}$, where subscript N indicates the C1 chondrite normalized value (Anders and Grevesse, 1989). To detect if any La enrichment occurred which may have caused an artefact in the Ce curve, we calculated the Pr/Pr* ratios, where $Pr/Pr^{*}=Pr_N/(0.5Ce_N+0.5Nd_N)$ (Bau and Dulski, 1996).

Scanning electron microscopy (both energy-dispersive spectroscopy (EDS) and backscattered electron microscopy (BSE)) was carried out in polished sections from six limestone samples, using a JEOL JXA-8600 Superprobe electron microscope (15 kV, 15 nA) at the Institute of Mineralogy and Geology, University of Miskolc.

Micromineralogy studies focused on sample KB-1. After dissolving the carbonate with 5 wt% acetic acid, the >45 μm fraction was sieved and the grains were inspected and picked under a stereo-microscope. To investigate the altered pyroxenes, amphiboles and clay spherules of the sample, scanning electron microscopy and EDS measurements were done in two laboratories. Secondary electron (SE) images were captured on a Hitachi S-4800 electron microscope (20 kV, 10 μA) at BAY-NANO (Miskolc). EDS and BSE images were obtained at the Department of Metallurgy, University of Miskolc, using an AMRAY-1860 T6 instrument (25 kV, 1–2 nA).

Whole rock mineral composition was determined and clay mineral investigations, including X-ray powder diffraction (XRD) measurements were done at the Institute of Mineralogy and Geology, University of Miskolc. The analyses were performed on a Bruker D8 Advance X-ray powder diffractometer (Bragg–Brentano geometry, Cu tube at 40 kV and 40 mA, 2°–65° (2θ), 0.04° step scanning, 2 s/step counting time, secondary graphite monocromator, fixed slit system of 0.6 mm primary-, 0.6 mm secondary- and 0.2 mm detector-slits, horizontal sample position, rotating sample holder), analyzed with EVA data handling program of the Bruker Diffrac*Plus* evaluation software package, full profile fitting, and a semi-quantitative method. Mineral species were identified based on the PDF2 (2005) database, except for clay minerals. Semi-quantitative evaluation was performed only after the identification of clay minerals by diagnostic procedures (Zajzon et al., 2012).

4. Results

4.1. Major element geochemistry

Changes in the ratio of terrigenous siliciclastic components are traceable through the analysis of Si, Al and CO_3 (Table 1). The two dominant detrital phases are quartz and clay minerals. The sum of $SiO_2+Al_2O_3$ is taken to represent the quantity of the siliciclastics, whereas the amount of clay minerals is tracked by Al_2O_3. Changes in the ratio of clay minerals and detrital quartz are thus reflected in the SiO_2 vs. Al_2O_3 curve (Fig. 3).

Above the limestone beds of Kössen Formation, in the boundary mudstone, the detrital component increases abruptly and significantly, and reaches a maximum in sample KB-4. From here its amount gradually decreases upsection. The clay content is also highest in the boundary mudstone, and higher up quartz becomes more abundant among the detrital components.

The iron content is the lowest (0.07 wt% Fe_2O_3) in the pure limestones of the Kössen Formation. The other limestone interbeds higher in the section contain around 0.5 wt% Fe_2O_3. Much higher Fe content, typically between 3 and 4 wt%, is registered in the boundary mudstone (with peak values of 5.29 and 5.78 wt% in samples KB-4 and KB-8, respectively). The Jurassic marl interbeds usually contain 2–3 wt% Fe_2O_3.

The sulfur content in the section is low, except for the lower part of boundary mudstone and two other marl layers which contain more than 0.5 wt%. The sulfur content and partly also the iron in the samples is hosted by the pyrite and gypsum phases.

4.2. Redox-sensitive minor and trace elements

4.2.1. Redox-sensitive elements

The redox-sensitive elements such as Mo, Cd, V, U, Mn and other chalcophile elements (As, Sb, Sn and Cu) tend to concentrate in reducing environments in the form of sulphides or are absorbed in organic compounds (Berner, 1971; Calvert, 1976, Dolenec et al., 2001). To filter out the dilution effect of the carbonate fraction on the signal, the measured values were normalized to Th, which is regarded as an element of the terrigenous component not controlled by the redox state of the depositional environment. Concentration of the redox-sensitive elements remain low throughout the section (Table 1, Fig. 4). Enrichment in these elements occurs only in the lowermost 10 cm of the boundary mudstone (samples KB-1, 2 and 3).

4.2.2. U/Th ratio

Although uranium and thorium are similar elements, their behavior is different in reducing and oxidative environments. Thorium is not sensitive to the redox conditions, whereas uranium is precipitated and concentrated only in reducing regimes. Oxidative bottom waters cause U to remain dissolved, hence the sediment would become depleted with respect to U. The PAAS (“Post-Archean Australian Shale” standard, thought to represent the upper continental crust) has a U/Th value of 0.26 (McLennan, 1989), whereas that of the C1 chondrite is 0.27 (Anders and Grevesse, 1989). Generally, a U/Th ratio >0.5 is taken to signal anoxic environment (Adams and Weaver, 1958; Fisher and Wignall, 2001; Myers and Wignall, 1987). The U/Th ratio remains low in most of the studied section, except between the samples KBL-K2 and KB-3, where it increases up to 8.5. Significantly, most of the $\sim$2 m thick boundary mudstone, except for its lowermost

Table 1
Data of major and trace element chemical analyses.

Sample No.↓	C (%)	Al_2O_3 (%)	SiO_2 (%)	P_2O_5 (%)	S (%)	CaO (%)	Fe_2O_3 (%)	V (ppm)	Cu (ppm)	Zn (ppm)	As (ppm)	Mo (ppm)	Cd (ppm)	Sn (ppm)	Sb (ppm)	Th (ppm)	U (ppm)	LOI (%)	Sum (%)
det. limit→	0.02	0.01	0.01	0.001	0.02	0.01	0.04	8	0.1	1	0.5	0.1	0.1	1	0.1	0.2	0.1		
KBL-28	12.84	0.46	1.95	0.019	0.04	53.11	0.17	20	1.9	6	2.0	0.3	0.1	<1	<0.1	0.9	2.6	43.0	99.70
KBL-26	12.81	0.42	2.27	0.004	0.14	52.58	0.42	13	0.7	3	16.1	9.1	<0.1	<1	0.1	1.0	5.1	42.6	99.13
KBL-25	12.13	1.15	5.27	0.010	0.02	50.02	0.50	18	1.5	3	3.3	0.4	<0.1	<1	<0.1	1.1	2.8	41.5	99.54
KBL-23	11.79	1.32	6.53	0.037	0.22	49.16	0.62	22	2.2	4	2.2	1.0	<0.1	<1	<0.1	1.8	2.2	40.5	99.64
KBL-22	11.77	1.55	6.12	0.042	0.03	48.94	0.87	22	3.3	7	2.7	0.3	<0.1	<1	<0.1	1.3	2.2	41.1	100.02
KBL-21	11.98	1.23	5.33	0.014	0.03	50.43	0.50	<8	1.9	3	0.9	0.2	<0.1	<1	<0.1	1.1	1.3	41.7	100.27
KBL-20	11.93	1.37	6.16	0.032	<0.02	49.38	0.52	<8	2.2	3	1.5	0.1	<0.1	<1	<0.1	1.5	1.5	41.1	99.74
KBL-19	11.73	1.16	7.04	0.062	0.03	49.63	0.51	<8	1.4	3	1.1	0.6	<0.1	<1	<0.1	1.3	1.2	40.7	100.39
KBL-18	11.65	1.05	6.29	0.021	0.02	50.13	0.62	<8	2.4	3	2.2	0.4	<0.1	<1	<0.1	1.4	1.4	41.1	100.42
KB-36	7.16	7.00	28.72	0.050	0.20	29.49	2.88	41	9.3	16	6.0	0.5	0.1	1	0.1	7.4	3.5	28.4	99.96
KBL-17	11.67	1.25	6.51	0.012	0.04	50.13	0.51	<8	1.4	2	0.8	0.1	<0.1	<1	<0.1	1.2	1.4	41.2	100.88
KB-35	7.30	7.59	25.91	<0.001	0.10	31.00	2.21	49	9.6	18	3.9	0.1	0.1	1	<0.1	7.0	3.0	29.7	99.96
KBL-16	11.83	1.47	7.12	0.017	0.02	49.52	0.51	9	1.7	3	0.7	<0.1	<0.1	<1	<0.1	1.4	1.2	40.5	100.37
KB-34	10.14	3.20	12.39	<0.001	0.01	44.18	0.99	19	3.7	7	1.5	0.1	<0.1	1	<0.1	2.5	1.2	37.5	99.99
KBL-15	11.82	1.39	6.54	0.025	<0.02	49.88	0.41	10	1.5	3	1.0	0.1	<0.1	<1	<0.1	1.2	0.8	41.1	100.59
KB-33	5.73	9.27	35.42	0.040	0.01	23.01	3.04	49	12.4	23	2.9	0.2	0.1	2	<0.1	7.2	2.4	24.9	99.87
KB-31	7.03	7.59	29.24	0.020	0.45	28.95	2.21	45	9.1	18	2.4	0.4	0.2	1	<0.1	6.6	2.8	28.1	99.87
KBL-14	12.15	0.80	5.68	0.048	0.04	51.24	0.40	<8	1.3	2	1.1	0.5	<0.1	<1	<0.1	0.9	1.7	41.2	100.48
KB-30	8.59	5.83	22.10	0.020	0.01	34.64	2.26	37	8.9	15	3.7	0.5	0.1	1	<0.1	6.7	3.6	32.1	99.85
KBL-13	12.14	0.98	5.80	0.014	0.24	50.44	0.50	<8	1.4	2	1.1	0.3	<0.1	<1	<0.1	1.0	1.5	41.4	100.37
KBL-12	12.31	0.94	5.33	0.024	0.06	51.29	0.41	<8	1.7	2	0.6	0.2	<0.1	<1	<0.1	1.0	1.8	41.4	100.52
KB-28	6.17	9.06	31.37	0.030	0.01	25.38	3.02	52	13.4	22	4.2	0.3	0.1	2	<0.1	8.7	3.6	26.9	99.86
KBL-11	11.90	1.19	6.30	0.009	0.10	49.84	0.43	9	1.4	3	1.2	0.1	<0.1	<1	<0.1	1.2	1.3	41.1	100.11
KBL-10	12.14	1.00	5.35	0.019	0.05	50.77	0.50	<8	1.2	2	1.1	0.3	<0.1	<1	<0.1	1.1	1.4	41.4	100.20
KB-26	8.24	5.95	22.58	0.030	0.01	34.23	2.28	34	9.8	16	3.3	0.3	0.3	1	0.1	7.2	2.9	31.8	99.87
KBL-9	12.29	0.95	4.48	0.022	0.07	51.21	0.39	<8	0.8	3	1.0	<0.1	<0.1	<1	<0.1	0.6	1.4	41.7	99.91
KBL-8	12.51	0.75	3.51	0.031	0.03	51.78	0.33	<8	1.3	2	<0.5	0.1	<0.1	<1	<0.1	0.8	1.4	42.4	100.00
KB-25	10.05	3.65	15.47	<0.001	0.09	41.01	1.74	23	7.4	12	2.0	0.6	0.2	1	<0.1	4.7	3.2	35.7	99.86
KBL-7	11.89	1.12	4.85	0.009	0.14	51.32	0.38	8	1.5	3	1.0	0.2	<0.1	<1	<0.1	1.1	1.6	41.6	100.49
KB-23	8.38	5.25	22.52	0.020	0.01	35.45	2.05	31	8.3	13	1.8	0.3	0.1	1	<0.1	6.2	2.7	31.9	99.95
KBL-6	12.11	1.28	6.32	0.015	0.09	49.97	0.48	10	1.8	3	1.2	0.2	<0.1	<1	<0.1	1.1	1.1	40.6	99.98
KB-22	8.38	5.23	21.98	0.030	0.01	35.81	1.92	33	8.0	12	1.4	0.4	0.1	1	0.1	6.1	2.5	32.2	99.94
KB-21	8.13	5.11	22.61	0.030	0.01	35.50	2.09	30	8.8	12	1.5	0.4	0.1	1	<0.1	5.9	2.8	31.9	99.93
KBL-4	11.97	1.20	5.35	0.057	0.04	50.61	0.47	9	1.6	3	0.8	0.1	<0.1	<1	<0.1	1.4	1.6	41.1	100.13
KB-20	8.13	5.72	28.13	0.020	0.65	32.00	2.16	40	9.6	17	2.2	0.5	0.1	1	<0.1	6.3	3.1	28.8	99.87
KB-19	7.34	6.54	30.05	0.030	0.01	29.67	2.34	40	10.6	16	2.3	0.3	0.1	1	<0.1	7.0	2.9	28.1	99.95
KBL-3	12.01	1.17	4.87	<0.001	<0.02	51.94	0.46	9	1.6	3	0.8	<0.1	<0.1	<1	<0.1	1.4	1.1	41.4	100.80
KB-18	5.56	9.22	35.66	0.030	0.01	23.06	3.20	56	15.6	20	2.6	0.2	0.1	2	0.1	9.0	2.8	24.7	99.97
KBL-2	11.76	1.52	6.33	0.028	0.03	49.79	0.67	12	2.0	6	1.1	<0.1	<0.1	<1	<0.1	1.4	2.0	41.1	100.73
KB-17	3.95	10.88	44.26	0.050	0.02	16.27	4.00	70	17.3	36	4.8	0.1	0.1	2	0.1	12.2	2.8	19.9	99.95
KBL-1	11.39	2.15	8.00	0.015	0.03	47.87	0.81	17	3.2	6	0.9	<0.1	<0.1	<1	<0.1	1.9	1.7	40.1	100.29
reKB-15	4.15	11.00	42.46	0.070	0.03	17.39	3.87	69	11.3	28	5.2	0.1	0.2	2	0.1	9.2	3.8	20.5	99.96
KB-15	4.21	11.03	42.31	0.090	0.03	17.50	3.95	74	11.3	28	4.6	0.1	0.1	2	<0.1	11.4	4.0	20.4	99.94
KB-14	1.58	18.07	50.25	0.070	0.02	6.17	3.71	113	22.0	19	1.1	<0.1	<0.1	3	<0.1	13.1	2.1	14.8	99.85
KB-13	1.44	18.76	50.87	0.050	0.01	5.86	3.52	117	22.6	19	1.0	<0.1	<0.1	4	<0.1	14.2	2.0	14.2	99.97
KB-12	1.31	19.18	50.83	0.060	0.02	5.08	4.08	122	25.1	23	1.3	<0.1	<0.1	4	<0.1	14.7	2.7	14.0	99.96
KB-11	1.60	19.26	48.46	0.050	0.04	6.67	3.83	120	23.8	21	1.9	0.1	<0.1	4	<0.1	16.0	2.3	15.3	99.97
KB-10	1.13	19.09	51.44	0.070	0.03	4.50	4.29	116	23.8	24	3.9	0.1	0.1	4	<0.1	17.0	2.4	14.0	99.96
KB-9	2.67	13.78	51.16	0.080	0.01	10.44	3.27	98	16.7	21	3.8	<0.1	0.1	3	0.1	12.5	2.6	15.5	99.96
KB-8	0.97	19.33	52.18	0.060	0.52	3.75	5.78	124	23.1	30	1.9	0.4	0.1	4	0.1	16.0	3.1	12.8	99.84
KB-7	1.15	19.46	51.23	0.050	0.51	4.63	4.62	120	23.2	30	2.6	0.2	0.2	4	0.1	16.4	3.1	13.6	99.82
KB-6	3.34	12.33	47.70	0.060	0.45	12.12	3.49	88	15.6	49	3.0	0.3	0.2	3	0.1	11.5	2.3	17.3	99.83
KB-5	3.82	11.74	47.49	0.060	0.76	13.78	3.95	96	17.0	61	6.6	0.5	0.4	3	0.2	12.6	3.2	17.4	99.97
KB-4	3.04	15.88	51.30	0.060	0.67	7.31	5.29	138	29.3	61	12.9	1.0	0.7	4	0.4	15.2	5.2	15.1	99.94
KB-3	7.42	6.22	22.39	2.720	0.03	33.48	3.14	64	16.0	90	8.1	1.4	1.1	2	0.6	6.5	12.6	29.4	99.74
KB-2	12.81	1.48	7.05	1.190	0.04	46.42	2.78	30	13.4	106	8.5	1.6	1.4	<1	0.8	1.3	7.0	39.5	99.80
KB-1	12.81	0.58	2.62	0.030	<0.01	53.06	1.09	11	1.4	4	6.1	1.7	0.1	<1	0.2	0.6	1.6	41.7	99.87
KBL-0	12.62	0.37	2.50	0.040	0.03	52.90	1.36	9	1.2	8	4.2	1.2	0.2	<1	0.3	0.4	1.3	42.4	100.30
KBL-K2	12.92	0.15	0.58	0.008	0.02	55.23	0.07	<8	0.5	3	0.6	<0.1	<0.1	<1	<0.1	0.2	1.7	43.2	100.00
KBL-K3	13.06	0.09	0.35	0.018	0.02	56.23	0.07	<8	0.2	5	0.6	0.1	0.2	<1	<0.1	<0.2	2.0	43.2	100.52

part, yielded consistently low U/Th values. High values return only in the upper part of the studied section, where the U/Th ratio in several limestone layers (KBL-25, 26, 28) exceeds 2.

4.2.3. Cerium anomaly

Several studies demonstrated that the redox sensitivity of Ce is a useful indicator of paleoceanographic conditions (DeBaar et al., 1985, 1988; Elderfield, 1988; German et al., 1995; Hu et al., 1988; Sholkovitz and Schneider, 1991; Schijf and DeBaar, 1995; Dolenec et al., 2001). The abundance of Ce of the carbonate phase in carbonate rocks directly reflects the Ce concentration of the seawater, which in turn is a good indicator of the redox state of the environment. Cerium enters the ocean in its soluble, trivalent state but under oxic bottom water conditions, Ce becomes relatively depleted, as its oxidized

form, Ce(IV) is quickly precipitated from the water (Elderfield, 1988; Dolenec et al., 2001), causing a negative Ce anomaly in the REE pattern of the marine carbonates (Dolenec et al., 2001; Hu et al., 1988). However, under anoxic conditions, the behavior of Ce will be similar to other trivalent REE. Thus in the REE pattern of the carbonate phase no pronounced negative Ce anomaly will be visible, resulting a largely flat REE pattern (Dolenec et al., 2001). This can be represented with the Ce/Ce* ratio.

In the studied section the Ce/Ce* curve shows an opposite redox signal to the minor redox sensitive elements (Fig. 4). REE measurements could only be performed in the whole-rock samples, not in the separated carbonate fractions. In this case the terrigenous REE content is more dominant in the signal than the carbonate REE, which can be seen in the three-four times higher ∑REE of the marls, compared to the carbonates. The Ce-depletion is explained by the dissolution of Ce from the terrigenous component, and staying in the anoxic sea-water, causing an opposite pattern to that seen in the carbonate fraction.

The Ce/Ce* is around 0.9 in the marls and 0.75 in the limestone beds. The difference between them is coming from the different terrigenous/carbonate ratio. The carbonate fraction contains a more depleted value, which suggests oxygenated bottom water in the section. Samples from the Kössen Formation yielded more depleted values (0.5) than the Kendlbach Formation limestones, which is explained by the higher carbonate content, and also reflects oxygenated water. The only samples which deviate from this trend are KB-1, 2 and 3. Even though they have lower carbonate content than KBL-K3 and 2, they have more depleted Ce/Ce* values (0.33–0.36).

To check if the Ce/Ce* value is not an artifact of positive La enrichment, the Pr/Pr* value was calculated (Bau and Dulski, 1996). The values do not show La enrichment.

4.3. Rare earth elements (REE)

The normalized REE patterns of most samples are remarkably similar to each other and resemble a presumed typical continental source rock (Table 3, Fig. 5). Three features of the REE patterns warrant further discussion: the occasional presence of a Ce-anomaly, HREE enrichment in two samples, and the systematically lower REE content of the limestone samples as compared with the marls. The majority of the observed anomalies are confined to the basal part of the section.

The two stratigraphically lowermost samples (KBL-K2 and KBL-K3) from the upper part of the Kössen Formation have the lowest amount of REE, but their overall pattern is similar to that of the others. These samples are from the purest limestone with the lowest amount of terrigenous material.

The next layer is the topmost limestone bed of the Kössen Formation (represented by duplicate samples KBL-0 and KB-1, yielding the same results), which shows a significant HREE enrichment.

Sample KB-2 was obtained from the 5 cm thick marl layer directly overlying the Kössen Limestone. The abundance of REE in this sample is comparable to most others and some HREE enrichment is also present here but less pronounced than in the underlying layer.

Sample KB-3 is from a brown, marly layer that contains scattered fish remains (scales and bone fragments). This is reflected in the high apatite content, determined by XRPD as 4 wt%, and the high concentration of P_2O_5, determined by whole-rock chemistry as 2.72 wt% (Tables 2 and 3). The presence of apatite might explain the unusual abundance of REE in this sample, 1.5–3 times higher than in most of the other marl samples, making this sample the richest in REE in the entire studied section. However, there is no HREE enrichment in this sample, contrary to samples KB-1 and KB-2.

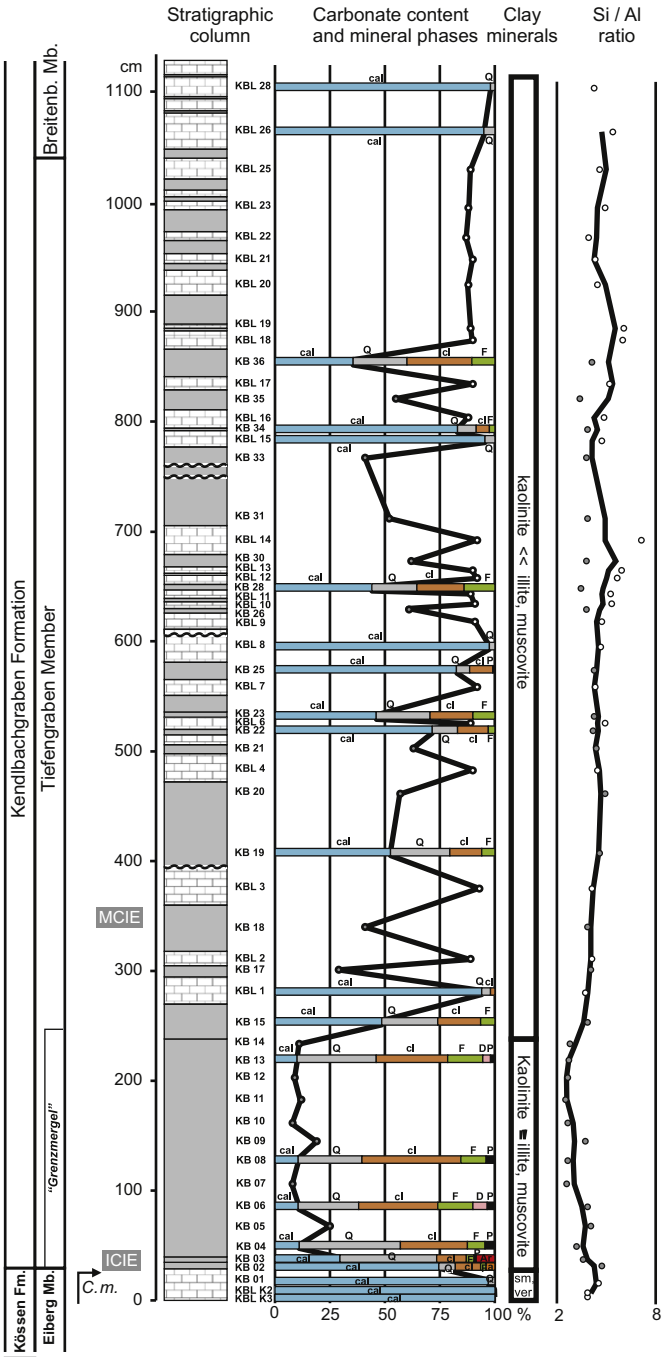

Fig. 3. Stratigraphy, mineral composition, and Si and Al elemental geochemistry of the Kendlbachgraben section. Sampled horizons are marked and labeled along the lithologic column. Horizontal bars show carbonate content and other mineral phases from XRD. Colors (and abbreviations) for mineral phases of the samples: blue (cal)–calcite, gray (Q)–quartz, brown (cl)–clay minerals, green (F)–feldspar, black (P)–pyrite, orange (a)–apatite, red (Ar)–aragonite, pink (D)–dolomite. The curve in the same panel shows changes in the carbonate content measured by XRD or from the chemical analyses (circles). Main changes in clay mineralogy are indicated. Panel to the right shows the Si/Al ratio (on logarithmic scale). Solid markers denote marl samples, open markers denote limestone samples. ICIE: Initial carbon isotope excursion. MCIE: Beginning of the main carbon isotope excursion. Line with arrowhead marks the last occurrence datum of *Choristoceras marshi* (*C. m.*). (For interpretation of the references to color in this figure legend, the reader is referred to the web version of this article.)

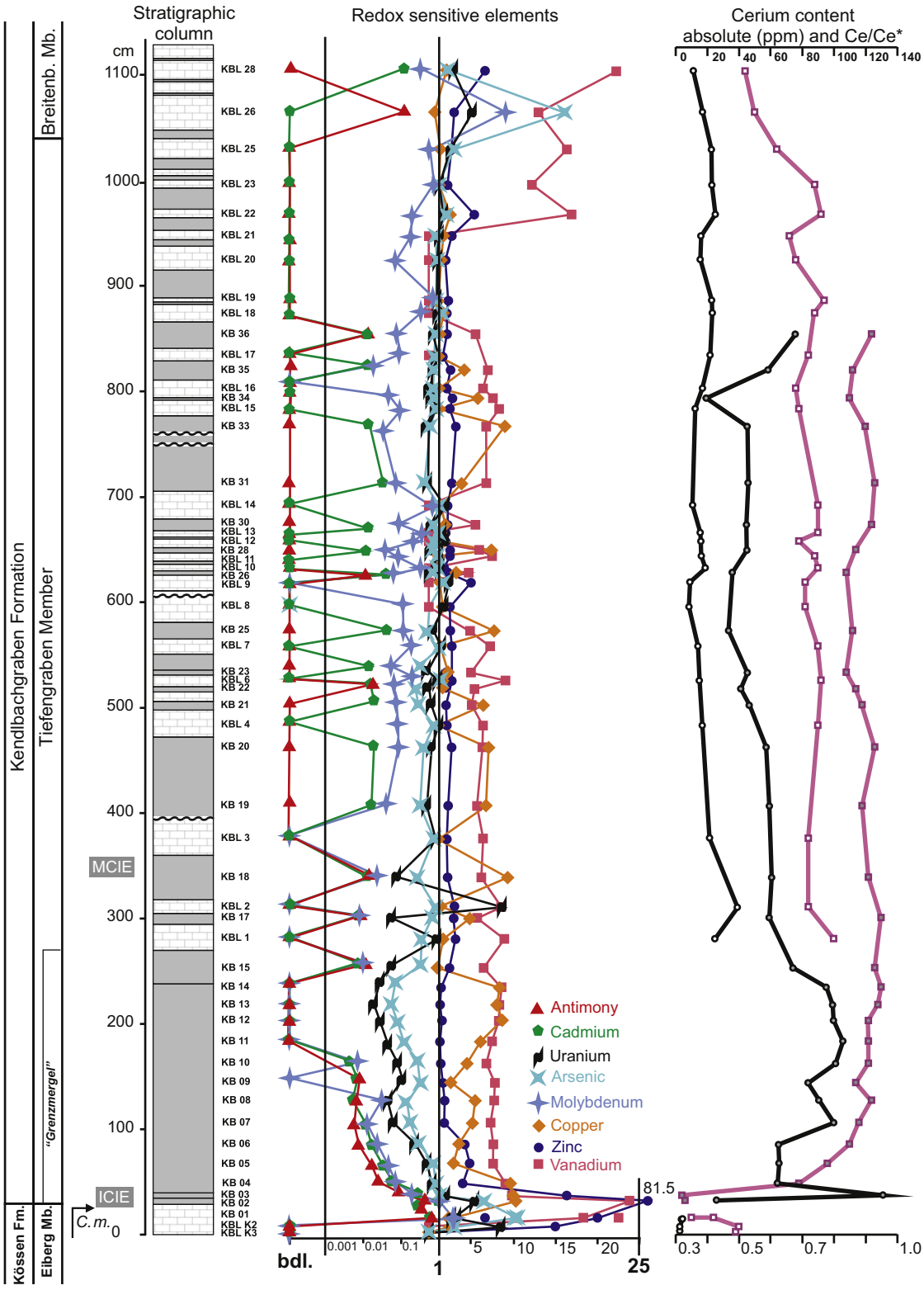

Fig. 4. Stratigraphy, and minor and trace elemental geochemistry of the Kendlbachgraben section. Sampled horizons are marked and labeled along the lithologic column. Panels to the right show Th-normalized values of redox-sensitive elements (note the combined scale: bld–below detection limit, logarithmic (0.001–1), normal (1–25), value shown >25), Ce content (in ppm, upper scale, black line), and Ce/Ce* (lower scale, purple line). Solid markers denote marl samples, open markers denote limestone samples. ICIE: Initial carbon isotope excursion. MCIE: Beginning of the main carbon isotope excursion. Line with arrowhead marks the last occurrence datum of *Choristoceras marshi* (*C. m.*).

Starting from sample KB-4, the REE content and REE pattern of the samples are remarkably similar to each other. The only significant difference is that the marly samples contain approximately three times more REE than the limestones. This observation agrees well with the three-to-four times higher amount of detrital terrigenous material in the marls, as calculated from the carbonate content of the samples.

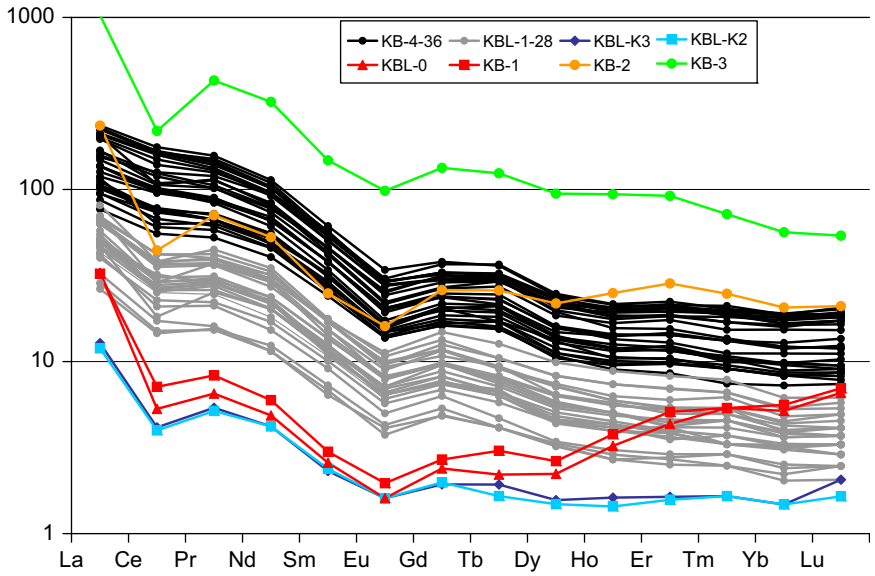

Fig. 5. Chondrite-normalized REE distribution patterns (spider diagrams) from the Kendlbachgraben section. Colored lines and larger markers denote samples explained in the text and named in the legend, gray lines refer to all other limestone samples, black lines refer to all other marl samples. (For interpretation of the references to color in this figure legend, the reader is referred to the web version of this article.)

4.4. Mineralogy

4.4.1. Mineral phases from X-ray diffraction

Mineral phases were identified in 22 samples from the section using X-ray powder diffraction (XRPD). Nine samples were further investigated for an in-depth characterization of their clay mineral content, the details of which are beyond the scope of this paper and are presented elsewhere (Zajzon et al., 2012). The results are summarized here in Table 3 and Fig. 3.

The three main components of the samples are calcite, quartz and clay minerals, beside some less abundant phases such as pyrite, feldspar, apatite, aragonite, gypsum and dolomite. The purest limestone occurs in the Kössen Formation. In the overlying boundary mudstone, the carbonate content drops to 10 wt%. Quartz, clay minerals, feldspars and pyrite appear here as phases not encountered lower in the section. The highest clay mineral content, recorded in sample KB-8, is 45 wt%.

The occurrence of pyrite is characteristic for the boundary mudstone, although it is also found at other levels higher in the section. The FeO content of the samples correlates well with the pyrite and goethite phases. The majority of the pyrite is framboidal, as revealed by SEM, indicative of bacterial origin (see below in Section 4.4.3.). The oxidation of pyrite led to formation of gypsum. The alteration may have occurred either in the outcrop or later, after sample collection. Sample KB-2 contains 4 wt% fluorapatite, which is bound to the unusually abundant fish remains (bones, teeth, scales) in this layer. Sample KB-3 contains 8.4 wt% of aragonite, which likely represents the original shell material of bivalves and foraminifera.

The feldspar phases present are albite, sanidine and microcline. The highest amount is registered in the middle to upper part of the boundary mudstone, reaching up to 16 wt%. Sanidine occurs only in the upper part of the boundary mudstone. Dolomite appears in only two samples, accompanied in both by sanidine.

4.4.2. Clay mineralogy

In the majority of samples, illite and kaolinite are registered as the main clay minerals with subordinate smectite, and their ratios were monitored to allow environmental and paleoclimatic inferences. Sample KB-1, however, shows a peculiar clay mineral composition very different from the other samples, because it is dominated by low- to medium-charged smectite and also contains vermiculite. These clay minerals commonly represent the alteration products of mafic and/or ultramafic rocks. Upsection, in the boundary mudstone, the clay mineral distribution is characterized by kaolinite ≥ illite + muscovite » smectite. In the higher part of the section a distinctive change in the clay mineral pattern results in illite + muscovite»kaolinite»smectite ratios. For more detail, see Zajzon et al. (2012).

4.4.3. Scanning electron microscopy (SEM) of pyrite

Six polished samples (KB-1, KBL-K3, 1, 8, 15, 26) were selected for investigation by SEM. All of these samples contain a varying amount of pyrite, which is dominantly framboidal. In some of the samples only goethite pseudomorphs were observed, but their shape clearly identifies them as alteration products from pyrite. In many instances the shell of a fossil or part of a microbial mat is recognizable as the locus of pyrite formation. Pyrite also frequently occurs together with apatite. Beside the framboidal form, euhedral pyrite is also common in the samples and both varieties may occur in distinct layers. The framboids are commonly large (0.1–0.2 mm in diameter), and form structures such as mats and spheres, indicative of their formation in the sediment rather than in the water column (Wignall and Newton, 1998; Wilkin et al., 1996). Barite was also found in some layers (e.g. sample KBL-26).

4.4.4. Micromineralogy of sample KB-1

To follow up on the indication of a possible mafic detrital component suggested by REE data and clay mineralogy, sample KB-1 from the topmost layer of the Kössen Formation was subjected to heavy mineral separation and SEM/EDS examination. The grain size of this micritic limestone is very fine, not more than a few wt% is above 45 μm of the insoluble part. Possible alteration products of volcanic material were indeed detected in this sample, in the form of goethite pseudomorphs after euhedral crystals of pyroxene and amphibole, and pale-green clay spherules that may represent altered glass (Fig. 6).

No fresh magmatic minerals were observed, only their alteration products. Goethite pseudomorphs are common, retaining the

Table 2
Data of REE chemical analyses.

Sample No.↓	La	Ce	Pr	Nd	Sm	Eu	Gd	Tb	Dy	Ho	Er	Tm	Yb	Lu
det. limit→	0.1	0.1	0.02	0.3	0.05	0.02	0.05	0.01	0.05	0.02	0.03	0.01	0.05	0.01
KBL-28	11.1	11.0	2.25	9.2	1.73	0.40	1.88	0.29	1.53	0.31	0.84	0.13	0.63	0.10
KBL-26	16.5	17.4	3.31	14.5	2.55	0.63	2.92	0.46	2.40	0.49	1.31	0.19	1.00	0.15
KBL-25	19.0	23.0	3.99	15.8	2.61	0.60	2.63	0.38	2.01	0.41	1.11	0.16	0.86	0.13
KBL-23	14.8	22.7	3.56	14.4	2.52	0.54	2.31	0.34	1.75	0.33	0.85	0.13	0.71	0.11
KBL-22	16.4	25.3	3.75	15.1	2.49	0.56	2.31	0.33	1.73	0.33	0.86	0.13	0.73	0.12
KBL-21	12.8	15.9	2.52	10.3	1.76	0.34	1.45	0.23	1.06	0.22	0.61	0.08	0.50	0.07
KBL-20	11.7	15.4	2.45	9.2	1.65	0.36	1.52	0.23	1.11	0.23	0.56	0.09	0.52	0.07
KBL-19	14.8	22.5	3.26	13.1	2.09	0.46	1.91	0.28	1.38	0.28	0.67	0.11	0.63	0.09
KBL-18	15.4	23.0	3.48	13.7	2.51	0.52	2.12	0.34	1.56	0.32	0.79	0.12	0.65	0.10
KB-36	36.2	76.0	10.66	42.1	7.88	1.65	6.30	1.09	4.72	0.87	2.46	0.33	1.98	0.29
KBL-17	15.1	21.4	3.23	12.3	2.27	0.45	1.90	0.27	1.34	0.28	0.66	0.10	0.59	0.09
KB-35	32.0	58.1	7.94	29.6	5.63	1.12	4.65	0.78	3.43	0.66	1.96	0.25	1.59	0.25
KBL-16	13.5	17.4	2.72	10.0	1.74	0.39	1.61	0.24	1.17	0.24	0.61	0.08	0.53	0.08
KB-34	11.4	19.3	2.54	10.0	1.61	0.36	1.48	0.25	1.08	0.23	0.66	0.08	0.51	0.08
KBL-15	9.8	12.6	1.88	6.9	1.34	0.28	1.24	0.17	0.83	0.17	0.46	0.07	0.41	0.06
KB-33	23.7	45.2	5.94	21.8	3.91	0.77	3.20	0.57	2.54	0.53	1.54	0.22	1.36	0.20
KB-31	23.9	46.5	5.94	22.3	4.19	0.83	3.26	0.62	2.72	0.56	1.57	0.22	1.34	0.21
KBL-14	7.6	10.4	1.43	5.2	1.00	0.21	0.96	0.15	0.79	0.15	0.44	0.07	0.39	0.06
KB-30	22.2	44.4	5.96	23.4	4.72	0.93	3.89	0.70	3.18	0.58	1.66	0.22	1.34	0.21
KBL-13	10.7	15.7	2.32	9.1	1.68	0.36	1.48	0.24	1.12	0.24	0.61	0.08	0.53	0.08
KBL-12	12.0	16.2	2.53	9.8	1.82	0.40	1.73	0.26	1.30	0.27	0.73	0.11	0.62	0.09
KB-28	24.8	44.8	5.99	22.3	4.28	0.85	3.65	0.66	3.12	0.64	1.86	0.26	1.59	0.23
KBL-11	11.0	16.8	2.59	9.8	1.85	0.37	1.61	0.24	1.23	0.25	0.63	0.09	0.54	0.08
KBL-10	12.2	18.6	2.79	10.7	2.01	0.44	1.90	0.29	1.42	0.28	0.70	0.11	0.59	0.09
KB-26	20.4	36.5	5.18	20.7	3.76	0.79	3.36	0.58	2.72	0.54	1.56	0.22	1.35	0.19
KBL-9	6.7	9.1	1.36	5.2	0.94	0.23	0.95	0.15	0.81	0.16	0.43	0.06	0.36	0.06
KBL-8	6.2	8.8	1.38	5.6	1.07	0.24	1.05	0.15	0.78	0.15	0.40	0.06	0.33	0.05
KB-25	18.0	33.4	4.68	18.3	3.54	0.77	3.18	0.56	2.62	0.50	1.36	0.18	1.18	0.18
KBL-7	9.4	13.7	1.97	7.7	1.48	0.32	1.35	0.21	1.08	0.22	0.58	0.08	0.52	0.08
KB-23	26.1	45.9	6.44	25.2	4.57	0.90	4.09	0.72	3.36	0.70	1.91	0.24	1.60	0.23
KBL-6	10.1	15.2	2.19	8.2	1.58	0.34	1.45	0.23	1.08	0.24	0.62	0.09	0.52	0.07
KB-22	22.3	40.7	5.48	20.9	3.87	0.83	3.47	0.62	2.91	0.59	1.64	0.23	1.40	0.21
KB-21	24.9	47.0	6.33	24.4	4.75	0.92	4.02	0.76	3.32	0.67	1.84	0.25	1.55	0.22
KBL-4	11.9	17.7	2.64	10.7	1.99	0.45	1.94	0.30	1.55	0.31	0.83	0.12	0.69	0.10
KB-20	27.9	57.5	7.64	30.0	5.59	1.15	4.70	0.83	3.84	0.75	2.05	0.27	1.81	0.27
KB-19	32.2	59.9	7.84	31.3	5.56	1.14	4.89	0.89	3.90	0.80	2.27	0.32	1.98	0.29
KBL-3	15.7	22.0	3.34	13.4	2.26	0.50	2.28	0.33	1.80	0.35	0.95	0.15	0.78	0.12
KB-18	32.0	61.5	7.99	29.9	5.59	1.08	4.67	0.84	3.78	0.79	2.27	0.32	1.93	0.30
KBL-2	27.2	38.0	5.68	22.1	4.04	0.87	4.02	0.62	3.26	0.66	1.84	0.25	1.44	0.22
KB-17	29.7	59.3	7.44	27.7	5.01	0.97	4.27	0.77	3.60	0.78	2.33	0.32	2.09	0.33
KBL-1	15.9	25.5	3.55	13.6	2.55	0.54	2.47	0.38	2.00	0.41	1.10	0.16	0.88	0.14
reKB-15	37.2	71.9	9.06	35.0	6.79	1.41	6.21	1.11	5.28	1.11	3.25	0.45	2.71	0.42
KB-15	38.9	74.9	9.42	35.8	6.69	1.44	6.17	1.16	5.61	1.14	3.43	0.45	2.91	0.44
KB-14	48.7	95.9	11.85	43.5	7.48	1.56	5.84	1.08	4.82	0.98	2.92	0.41	2.65	0.40
KB-13	49.8	98.0	12.37	46.1	7.85	1.63	6.47	1.17	5.00	1.07	3.10	0.46	2.68	0.42
KB-12	52.4	99.2	12.77	46.1	8.43	1.62	6.45	1.16	5.49	1.08	3.20	0.46	2.93	0.47
KB-11	55.2	106.3	14.00	51.3	9.02	1.91	7.47	1.31	5.84	1.19	3.32	0.48	3.00	0.46
KB-10	53.1	101.1	13.03	47.1	8.34	1.63	6.47	1.18	5.74	1.10	3.23	0.47	3.05	0.46
KB-9	46.1	83.9	11.21	43.3	8.21	1.70	7.23	1.33	6.01	1.20	3.54	0.49	3.09	0.49
KB-8	47.1	90.2	11.53	41.5	7.41	1.54	5.95	1.13	5.27	1.12	3.28	0.45	2.93	0.45
KB-7	53.7	99.4	13.41	49.4	8.22	1.56	5.96	1.11	5.30	1.03	2.91	0.44	2.82	0.44
KB-6	34.9	64.2	9.11	33.3	6.17	1.21	5.22	0.99	4.49	0.93	2.77	0.37	2.49	0.37
KB-5	39.6	65.6	10.07	37.8	6.72	1.36	5.67	1.06	5.14	1.01	2.97	0.41	2.58	0.42
KB-4	48.3	64.3	10.18	36.6	6.33	1.24	5.30	1.06	5.22	1.15	3.38	0.51	3.05	0.50
KB-3	241.5	131.9	38.32	146.2	21.73	5.50	26.25	4.51	22.97	5.22	14.60	1.74	9.17	1.31
KB-2	55.2	26.7	6.31	23.9	3.66	0.90	5.12	0.94	5.28	1.39	4.52	0.60	3.35	0.51
KB-1	7.6	4.3	0.74	2.7	0.44	0.11	0.53	0.11	0.64	0.21	0.81	0.13	0.91	0.17
KBL-0	7.7	3.2	0.58	2.2	0.38	0.09	0.47	0.08	0.54	0.18	0.69	0.13	0.84	0.16
KBL-K2	2.8	2.4	0.46	1.9	0.35	0.09	0.39	0.06	0.36	0.08	0.25	0.04	0.24	0.04
KBL-K3	3.0	2.5	0.48	1.9	0.34	0.09	0.38	0.07	0.38	0.09	0.26	0.04	0.24	0.05

original shape of abundant pyroxene and subordinate amphibole crystals. These elongated grains are 0.1–0.2 mm in length, and the original crystal shape, the edges and facets are perfectly preserved (Fig. 6d–h). They are easily identifiable as three-dimensional grains in the acid insoluble residue. These pseudomorphs were also observed in the polished samples, where their recognition is more difficult because the shape of their cross-section is less distinctive and often similar to pseudomorphs after pyrite crystals.

Pale green, opaque or slightly transparent grains are also present in the sample. Their shapes vary, some of them are perfectly spherical whereas others are subangular (Fig. 6a–c). Their composition, as revealed by EDS, is illite/aluminoceladonite. The shape, size and composition together suggest that these grains represent alteration products of volcanic material, the spheres and rounded particles are most suggestive of altered volcanic glass spherules.

Table 3
Percent abundance of mineral phases from XRD analyses.

	Calcite	Quartz	Illite/muscovite	Kaolinite	Smectite	Albite	Sanidine	Microcline	Pyrite	Gypsum	Dolomite	Aragonite	Apatite-F
KBL-28	97.8	2.2											
KBL-26	95.2	4.8											
KB-36	35.7	24.3	22.4	5.4	1.5	5.0	5.7						
KB-34	82.8	8.9	3.1	2.1	0.4		2.6						
KBL-15	95.5	4.3			0.3								
KB-28	44.2	20.1	14.2	5.9	1.4	5.0	9.1						
KBL-8	97.3	2.7											
KB-25	82.7	5.8	7.9	2.1	0.5				1.1				
KB-23	45.9	24.5	12.8	5.6	1.0	5.7	4.6						
KB-22	71.4	11.7	11.2	2.0	0.9		2.7						
KB-19	52.4	27.1	10.6	3.5	0.4	5.8							
KBL-1	93.8	3.6	2.5		0.1								
KB-15	48.3	25.8	11.9	5.7	1.9	4.0		2.3					
KB-13	10.0	35.9	16.8	14.4	1.6	8.7		7.1	1.4	0.8	3.5		
KB-8	10.3	29.0	19.3	24.1	1.8			11.5	3.9				
KB-6	9.9	28.1	22.8	12.2	0.9	9.2	6.7		3.3	0.5	6.5		
KB-4	10.8	46.3	12.0	17.8	0.6	8.1			3.4	0.9			
KB-3	29.5	44.1	6.1	6.8	0.5	3.7			0.8			8.4	
KB-2	74.7	7.3	8.3	2.7	0.1	2.4							4.1
KB-1	96.8	3.2											
KBL-K2	100.0												
KBL-K3	100.0												

5. Discussion

5.1. Recorders of contemporaneous volcanism

Causal relationship of the ETE and coeval carbon cycle perturbation with CAMP volcanism has been proposed by many authors (e.g. Marzoli et al., 1999; Pálfy, 2003; Hesselbo et al., 2007). Support for this hypothesis is primarily provided by dating studies which have established with increasing precision and accuracy the synchrony between CAMP flood basalts (Marzoli et al., 1999, 2004; Nomade et al., 2007) and the Triassic–Jurassic boundary (Pálfy et al., 2000; Schaltegger et al., 2008; Schoene et al., 2010). However, direct stratigraphic evidence for CAMP-derived volcanic material in marine sections has been meager. Where CAMP flows or pyroclastics occur with marine sedimentary rocks, e.g. in France and Morocco, precise biostratigraphic dating is hampered by a lack of age-diagnostic fossils (Olsen et al., 2003). Recent studies in terrestrial sections using palynostratigraphy (Cirilli et al., 2009) and conchostracan biostratigraphy (Kozur and Weems, 2010) demonstrate that CAMP volcanism began in the latest Triassic. Available circumstantial evidence for the onset of volcanism include the presence of potentially volcanically derived organic molecules, polycyclic aromatic hydrocarbons, from TJB sediments (van de Schootbrugge et al., 2009) and increase in pCO_2 detected both in pedogenic carbonates (Schaller et al., 2011) and by fossil leaf stomatal density (McElwain et al., 1999; Steinthorsdottir et al., 2011).

In the Kendlbachgraben section, both the pyroxene and amphibole pseudomorphs and the altered glass spherules found in the topmost Kössen Formation (sample KB-1) are interpreted as volcanic eruption products, most likely representing a distal record of CAMP eruptions. The size and the well preserved rounded original shape of the altered glass spherules suggest airborne origin and transportation. The pyroxene and amphibole crystals fall into the fine ash size range, capable of entering the upper atmosphere within the eruption plume. The well preserved crystal facets and edges rule out the possibility of even short terrestrial transportation that would have caused wear and damage of the grains. The presence of all these "exotic" grains in the pure micritic limestone are best explained as air-fall fine ash particles directly deposited in the marine sedimentary basin.

In agreement with the above interpretation, the clay mineral pattern of this layer is also quite different from the other samples. It contains dominantly low- to medium-charged smectite as well as Mg-dominated vermiculite. Typically, these clay minerals occur as alteration products of mafic and ultramafic rocks (Velde and Meunier, 2008; see also Zajzon et al., 2012).

A third line of evidence is provided by the REE distribution patterns. The same sample (KB-1) from the topmost layer of Kössen Formation differs from all other samples by a distinctive enrichment of heavy REE. Only the overlying layer (sample KB-2) shows a similar, albeit more subdued HREE enrichment. Such trace element signature, characterized by a V-shaped pattern, may be best interpreted as a mixed signal where the light REEs are derived from the sedimentary component and the enrichement in HREE is sourced from magmatic material. HREE enrichment is characteristic for mantle sources and is known to occur, e.g. in N-MORB (Klein, 2003) and ultrabasic rocks (Bodinier and Godard, 2007), where it is carried by mineral phases such as garnets, pyroxenes and amphiboles. Pseudomorphs of the latter two minerals occur in the micromineralogical spectrum of the same sample.

The range of REE variation in CAMP extrusives have been reported in several studies and HREE enrichment is clearly documented by Marzoli et al. (2011) in the Preakness and Hook Mt. basalts in the Newark Basin, Sander basalt in the Culpeper basin, and the recurrent basalts in Morocco. The stratigraphic significance of this geochemical similarity to the late rather than early CAMP flows remains to be clarified.

To assess the feasibility of CAMP as a source of material preserved at Kendlbachgraben section, it is informative that paleogeographic reconstructions suggest an approximate distance of 2000–2500 km between northeastern CAMP eruptive centers and the marine Eiberg Basin in the western Tethys (Golonka, 2007). Volcanic particulates from eruption plumes are known to travel significant distances in downwind direction (Durant et al., 2010), as recently shown by widespread distribution of ash from the 2010 eruption of Eyjafjallajökull, clearly detected in the Alps, more than 2700 km from Iceland (Flentje et al., 2010). Climate modeling results suggest that the Eiberg basin was downwind of the CAMP at least seasonally during Pangean summers in the Triassic (Wang, 2009). Therefore emplacement of CAMP-derived

particles in sediments preserved at the Kendlbachgraben section appears plausible. The generally assumed quiet outpouring of flood basalts contradicts the here inferred explosive eruption, capable to produce a high eruption column necessary for long distance particle dispersal. We speculate that at least some of the CAMP volcanism may have been phreatomagmatic, where eruption fissures intersected lakes in the rift basin, thus resulting in unusually explosive eruptions. Because CAMP erupted in multiple pulses, further search for volcanic signatures, perhaps below the topmost Kössen Formation, is warranted to corroborate the evidence presented herein.

5.2. Climate-driven changes in detrital input and clay mineralogy

A first-order change in depositional regimes in the Kendlbachgraben section is manifest in the lithostratigraphic boundary between the intraplatform basinal carbonates of the Kössen Formation and clay-rich, fine silicilastics of the boundary mudstone of the Kendlbach Formation. The abrupt change from carbonate-dominated to siliciclastic-dominated sedimentation during the latest Rhaetian may be the stratigraphic expression of several factors. These include (i) a change in weathering regime, i.e. increased influx of terrigenous material and clay under hot and humid conditions, (ii) a biocalcification crisis that triggered a shutdown of the carbonate factory due to CO_2 saturation (Hautmann et al., 2008), (iii) loss of carbonate production due to eutrophication, (iv) rapid sea level rise manifested within a regression–transgression couplet (Hallam and Wignall, 1999), or (v) some combination of these factors.

Our major element and mineral phase distribution data allow quantification of these processes. The major drop in calcite content at the Kössen/Kendlbach formation boundary is clearly shown by XRD data (Table 3) and CaO and total C concentration (Table 1). The boundary mudstone has the highest ratio of clay minerals vs. other detrital components (mainly quartz), as expressed by the Si/Al ratio (Fig. 3) and XRD data (Table 3). Therefore, the initial increase of detrital components was accompanied by peak abundance of clay minerals, marking a significant climatic signal. Sudden climate change to hot and humid conditions leading to intensification of weathering may well explain the terrestrial influx. Co-occurrence of dolomite and feldspar in two samples in the boundary mudstone (KB-6 and 13) suggests further episodic increases in terrestrial input, whereby immature detrital components could reach the depocenter. The amount of the siliciclastic detritus decreases upsection, reflecting either a decrease in humidity and/or transgression and increasing distance from terrigenous source areas.

Clay minerals are well-known indicators of climate. In the boundary mudstone the clay mineral composition is kaolinite $\geq$ illite + muscovite $\gg$ smectite > chlorite. The predominance of kaolinite is commonly interpreted to suggest humid climate and intensive terrigenous input. Similar data are known from other TJB sections. Ahlberg et al. (2003) report a kaolinite $\approx$ illite $\gg$ chlorite and smectite (I/S) clay pattern from Rhaetian–Hettangian terrestrial sedimentary successions, and kaolinite $\approx$ illite > variable smectite $\gg$ chlorite pattern from shallow marine deposits (Höganäs Formation) in southern Sweden. These authors concluded that the original detrital composition was better preserved in the shallow marine settings and infer warm, humid conditions and intense weathering. High amounts of kaolinite are also reported from the topmost Triassic *Triletes* beds in Germany, interpreted to reflect strongly leached soils that become enriched in aluminum (van de Schootbrugge et al., 2009). A pronounced increase in kaolinite also characterizes the TJB in sections of the Tatra Mts. (Slovakia), where a climatic driver was similarly invoked (Michalík et al., 2010).

Higher up in the Kendlbachgraben section, above the boundary mudstone, the clay mineral pattern changes to illite + muscovite $\gg$ kaolinite $\gg$ smectite, which corresponds to a less humid and less hot climate. Therefore our results suggest that the extreme greenhouse conditions around the TJB were initially forced by volcanic CO_2 degassing but had a limited temporal extent, which nevertheless coincided with the ETE and the onset of both the initial and main negative carbon anomalies.

5.3. Changes in redox conditions

Marine anoxia often accompanies greenhouse climate maxima due to reduced ocean circulation, and plays a role in extinction events. Specifically, oxygen-depleted facies across the TJB were noted from northwest Europe (Hallam, 1995). Although no longer a favoured scenario, this possible cause is still often considered for the end-Triassic extinction (Hallam and Wignall, 1997). However, in sections in Britain, anoxic sediments were shown to occur only above the main end-Triassic extinction horizon and initial carbon isotope excursion (Wignall and Bond, 2008). Within our dataset, the occurrence of pyrite, distribution of redox-sensitive elements, and relative abundance of Ce among the other REE permit evaluation if dysoxic or anoxic conditions developed around the TJB in the Kendlbachgraben section.

Peak values of Fe and S within the boundary mudstone (see 4.1.) are tied to the occurrence of pyrite, as evidenced by XRD data (Table 3). SEM analyses reveal that framboidal pyrite of large size (up to 0.1–0.2 mm in diameter) is predominant, that suggests formation within the sediment under reducing conditions (Wignall et al., 2005), but it does not require the presence of anoxic bottom water.

Water column oxygenation is suggested by the redox-sensitive elements, whose concentration remains low throughout the section (Fig. 4). Enrichment of these elements is most pronounced in the lowermost 10 cm of the boundary mudstone (samples KB-1, 2 and 3), which are therefore permissive of reducing environment above the sediment/water interface. However, this observation contradicts the presence of benthic bivalves, but is compatible with the abundance of fish remains and phosphate in KB-3. A second interval with a somewhat elevated concentration of redox-sensitive elements is encountered near the top of the studied section, in the early Hettangian.

As an independent redox indicator, the U/Th ratio remains low in most of the studied section, except between the samples KBL-K2 and KB-3, where it goes up to as high as 8.5, possibly indicating oxygen-depleted conditions during deposition of the topmost Kössen Formation and the lowermost part of the boundary mudstone. This signal is comparable to that obtained by McRoberts et al. (1997) from another section in western Austria. Alternatively, the U/Th ratio at this level may also be influenced by volcanic input.

Interpretation of changes in Ce abundance in the section is not straightforward. As analyses were carried out on bulk samples, the Ce signal of marine carbonate is mixed with that of the detrital component. Higher carbonate content is correlated with negative shifts in Ce concentration, suggesting that the marine carbonate is depleted in Ce, which in turn points to oxidative water favoring precipitation of trivalent Ce. Anoxic bottom waters are not indicated by the Ce signal.

In summary, widespread anoxia near the TJB is not compatible with our data; oxygen-depleted bottom water may only characterized brief intervals during the earliest phase of boundary mudstone deposition, coinciding with the temperature maximum inferred from the clay mineral climate proxy. Several other sections in the Eiberg Basin contain the red Schattwald beds immediately below the TJB; this hematite-bearing unit

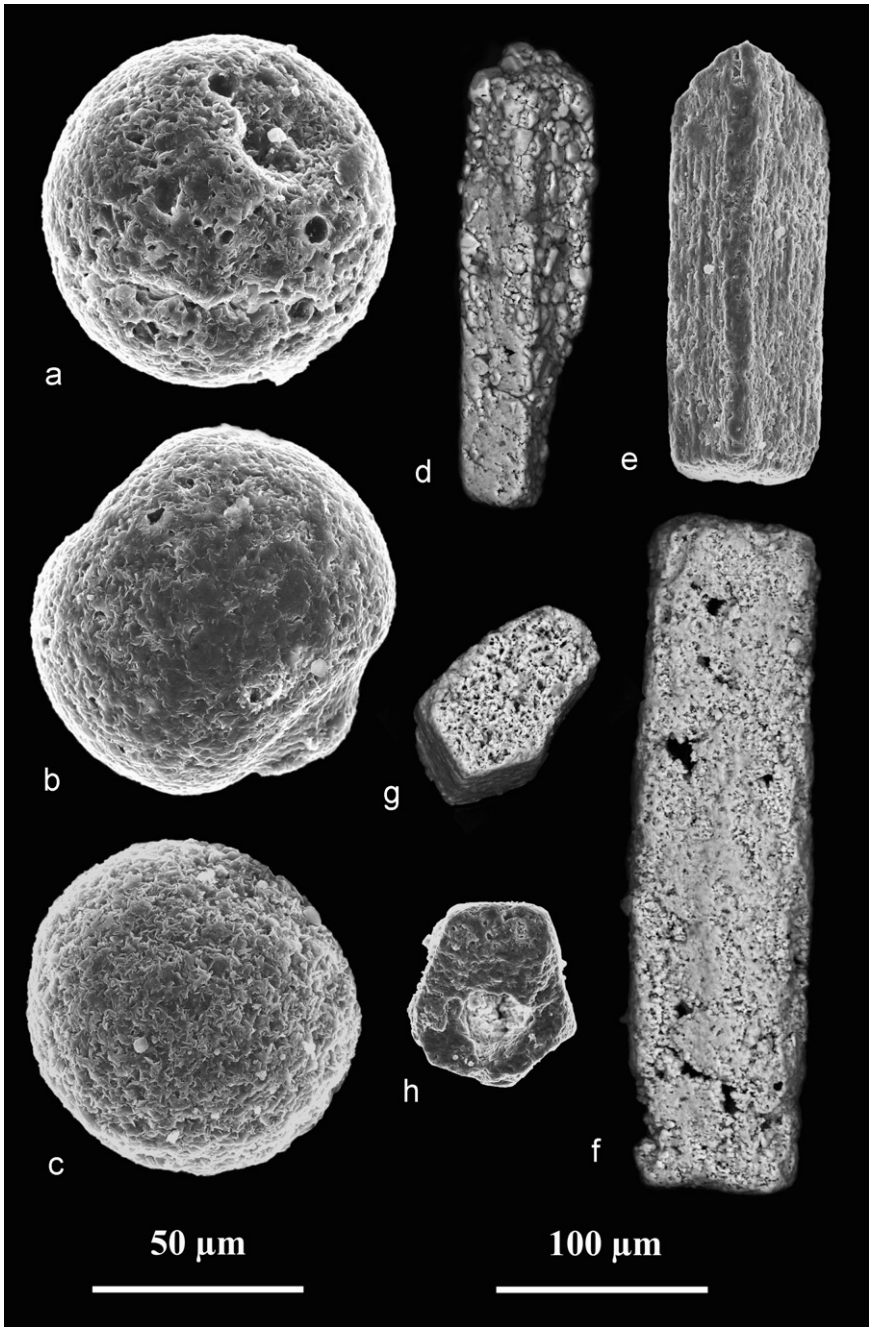

Fig. 6. SEM photomicrographs of assumed volcanically derived mineral grains from sample KB-1 (latest Triassic, from top of Kössen Formation). (a–c)—illite-aluminoceladonite spherules, presumed altered volcanic glass droplets; (d–f)—goethite pseudomorphs after pyroxene crystals; (g–h)—goethite pseudomorphs after amphibole crystals.

is a regional stratigraphic indicator of oxidized facies (Krystyn et al., 2005).

6. Conclusions

Our study has focused on a Triassic–Jurassic boundary (TJB) section at Kendlbachgraben in the Northern Calcareous Alps, within the same intraplatform basin as the recently selected base Jurassic Global Stratotype Section and Point. The much debated causation of the end-Triassic mass extinction (ETE) and broadly synchronous major carbon isotope excursions instigated our research. In particular, the aim of our multi-approach study was to search for stratigraphic evidence in this marine section for distant volcanism of the Central Atlantic Magmatic Province (CAMP), widely regarded as a trigger of interrelated global climatic, environmental and biotic changes. The key findings of our study are the following:

1. The topmost bed of the otherwise pure micritic limestone of the Rhaetian Kössen Formation contains goethite pseudomorphs of euhedral pyroxene and amphibole crystals. Such grains in this depositional environment are thought to represent distal fallout of a volcanic ash cloud.
2. The same bed also yielded rounded or spherical grains of illite/aluminoceladonite composition, interpreted as alteration products of airborne volcanic glass particles. Additional clay minerals restricted to this bed are low- to medium-charged

smectite and Mg-vermiculite, commonly formed by alteration of mafic volcanic material.

3. Another characteristic feature of this bed is its enrichment in heavy rare earth elements, a pattern noted from some mantle-derived mafic volcanics and documented from several flow units of the CAMP. This set of observed features is best explained by mafic volcanic material admixed to the carbonate from distal ash fallout, likely related to a CAMP eruption.
4. After the deposition of this layer, carbonate sedimentation of the Kössen Formation abruptly gave way to clay-rich, terrigenous sedimentation of the boundary mudstone and the overlying alternating mudstone, marl and marly limestone beds (topmost Rhaetian to lower Hettangian Tiefengraben Member of the Kendlbach Formation). Previous authors also noted the disappearance of Triassic ammonoid and conodont faunas and the onset of the initial carbon isotope excursion at this level. Thus this local facies change is best regarded as the record of far-reaching global changes immediately preceding the TJB, at the time of the ETE.
5. Elemental geochemistry and clay mineralogy helped quantify the increase in terrigenous and clay mineral input at the expense of carbonate production. The lowermost 2 m of the boundary mudstone is particularly rich in kaolinite, signifying a sudden change in weathering regime possibly related to transient extreme greenhouse climate in the hinterland.
6. Abundant framboidal pyrite is present in the TJB interval, but its size suggests formation within the sediment rather than in an anoxic water column. Redox-sensitive minor elements and Ce also fail to support widespread oxygen-depleted conditions in the marine basin. Thus anoxia does not appear to play a fundamental role in the extinction.

In summary, independent geochemical, micromineralogical and clay mineralogical lines of evidence provide as yet the best direct link between end-Triassic volcanism and the marine stratigraphic record, where extinction and the carbon isotope anomaly are also present. The new data provide further support for a scenario where CAMP volcanism induced climate and other environmental change which in turn triggered the ETE and is also reflected in the TJB carbon isotope anomalies.

Acknowledgments

Harald Lobitzer (formerly with the Austrian Geological Survey) is thanked for introducing us to the Kendlbach locality and arranging access with Austrian State Forests. Paul Wignall and two other anonymous journal reviewers are thanked for their constructive comments that improved the manuscript. Field work was supported by the Austrian–Hungarian Action Foundation, through a grant 51ÖU7. This study was financially supported by the Hungarian Scientific Research Fund (grants T42802 and K72633) and by the New Hungary Development Plan (grant TÁMOP-4.2.1.B-10/2/KONV-2010-0001). This is MTA-MTM-ELTE Paleo contribution No. 167.

References

Adams, J.A.S., Weaver, C.E., 1958. Thorium-to-uranium ratios as indicators of sedimentary processes: example of concept of geochemical facies. Am. Assoc. Petrol. Geol. Bull. 42, 387–430.

Ahlberg, A., Olsson, I., Šimkevičius, P., 2003. Triassic–Jurassic weathering and clay mineral dispersal in basement areas and sedimentary basins of southern Sweden. Sediment. Geol. 161, 15–29.

Alroy, J., 2008. Dynamics of origination and extinction in the marine fossil record. Proc. Natl. Acad. Sci. USA 105, 11536–11542.

Anders, E., Grevesse, N., 1989. Abundances of the elements: meteoritic and solar. Geochim. Cosmochim. Acta 53, 197–214.

Bau, M., Dulski, P., 1996. Distribution of yttrium and rare-earth elements in the Penge and Kuruman iron-formations, Transvaal Supergroup. South Africa Precambrian Res. 79, 37–55.

Berner, R.A., 1971. The synthesis of framboidal pyrite. Econ. Geol. 64, 383–384.

Bodinier, J.L., Godard, M., 2007. Orogenic, Ophiolitic, and Abyssal Peridotites. In: Heinrich, K.T., Karl, K.T. (Eds.), Treatise on Geochemistry. Pergamon, Oxford, pp. 1–73.

Bonis, N.R., Kürschner, W.M., Krystyn, L., 2009. A detailed palynological study of the Triassic–Jurassic transition in key sections of the Eiberg Basin (Northern Calcareous Alps, Austria). Rev. Palaeobot. Palynol. 156, 376–400.

Calvert, S.E., 1976. The mineralogy and geochemistry of nearshore sediments. In: Riley, J.P., Chester, R. (Eds.), Chemical Oceanography, vol. 6. Academic Press, New York, pp. 187–280.

Carter, E.S., Hori, R.S., 2005. Global correlation of the radiolarian faunal change across the Triassic–Jurassic boundary. Can. J. Earth Sci. 42, 777–790.

Cirilli, S., Marzoli, A., Tanner, L., Bertrand, H., Buratti, N., Jourdan, F., Bellieni, G., Kontak, D., Renne, P.R., 2009. Latest Triassic onset of the Central Atlantic Magmatic Province (CAMP) volcanism in the Fundy Basin (Nova Scotia): new stratigraphic constraints. Earth Planet. Sci. Lett. 286, 514–525.

DeBaar, H.J.W., Bacon, M.P., Brewer, P.G., Bruland, K.W., 1985. Rare earth elements in the Pacific and Atlantic oceans. Geochim. Cosmochim. Acta 49, 1943–1960.

DeBaar, H.J.W., German, C.R., Elderfield, H., Gaans, P.V., 1988. Rare earth element distributions in anoxic waters of the Carriaco Trench. Geochim. Cosmochim. Acta 52, 1203–1219.

Dolenec, T., Lojen, S., Ramovs, A., 2001. The Permian–Triassic boundary in Western Slovenia (Idrijca Valley section): magnetostratigraphy, stable isotopes, and elemental variations. Chem. Geol. 175, 175–190.

Durant, A.J., Bonadonna, C., Horwell, C.J., 2010. Atmospheric and environmental impacts of volcanic particulates. Elements 6, 235–240.

Elderfield, H., 1988. The oceanic chemistry of the rare-earth elements. Philos. Trans. R. Soc. Lond. Ser. A 325, 105–126.

Fisher, Q.J., Wignall, P.B., 2001. Palaeoenvironmental controls on the uranium distribution in an Upper Carboniferous black shale (*Gastrioceras listeri* Marine Band) and associated strata. England. Chem. Geol. 175, 605–621.

Flentje, H., Claude, H., Elste, T., Gilge, S., Köhler, U., Plass-Dülmer, C., Steinbrecht, W., Thomas, W., Werner, A., Fricke, W., 2010. The Eyjafjallajökull eruption in April 2010—detection of volcanic plume using in-situ measurements, ozone sondes and lidar-ceilometer profiles. Atmos. Chem. Phys. 10, 10085–10092.

Flügel, E., 2002. Triassic reef patterns. In: Kiessling, W., Flügel, E., Golonka, J. (Eds.), Phanerozoic Reef Patterns, 72. SEPM (Society for Sedmentary Geology) Special Publications, pp. 391–464.

Galli, M.T., Jadoul, F., Bernasconi, S.M., Cirilli, S., Weissert, H., 2007. Stratigraphy and palaeoenvironmental analysis of the Triassic–Jurassic transition in the western Southern Alps (Northern Italy). Palaeogeogr. Palaeoclimat. Palaeoecol. 244, 52–70.

German, C.R., Masuzawa, T., Greaves, M.J., Elderfield, H., Edmond, J.M., 1995. Dissolved rare earth elements in the Southern Ocean: cerium oxidation and the influence of hydrography. Geochim. Cosmochim. Acta 59, 1551–1558.

Golebiowski, R., 1990. Facial and faunistic changes from Triassic to Jurassic in the Northern Calcareous Alps (Austria). Cah. Univ. Cathol. Lyon, Sér. Sci. 3, 175–184.

Golebiowski, R., Braunstein, R.E., 1988. A Triassic/Jurassic boundary section in the northern Calcareous Alps (Austria). Ber. Geol. Bundesanst. 15, 39–46.

Golonka, J., 2007. Late Triassic and Early Jurassic palaeogeography of the world. Palaeogeogr. Palaeoclimat. Palaeoecol. 244, 297–307.

Guex, J., Bartolini, A., Atudorei, V., Taylor, D., 2004. High-resolution ammonite and carbon isotope stratigraphy across the Triassic–Jurassic boundary at New York Canyon (Nevada). Earth Planet. Sci. Lett. 225, 29–41.

Hallam, A., 1990. Correlation of the Triassic–Jurassic boundary in England and Austria. J. Geol. Soc. Lond. 147, 421–424.

Hallam, A., 1995. Oxygen-restricted facies of the basal Jurassic of northwest Europe. Hist. Biol. 10, 247–257.

Hallam, A., Goodfellow, W.D., 1990. Facies and geochemical evidence bearing on the end-Triassic disappearance of the Alpine reef ecosystem. Hist. Biol. 4, 131–138.

Hallam, A., Wignall, P.B., 1997. Mass Extinctions and Their Aftermath. Oxford University Press, Oxford.

Hallam, A., Wignall, P.B., 1999. Mass extinctions and sea-level changes. Earth-Sci. Rev. 48, 217–250.

Hautmann, M., 2004. Effect of end-Triassic CO_2 maximum on carbonate sedimentation and marine mass extinction. Facies 50, 257–261.

Hautmann, M., Benton, M.J., Tomasovych, A., 2008. Catastrophic ocean acidification at the Triassic–Jurassic boundary. N. Jb. Geol. Paläont. Abh 249, 119–127.

Hesselbo, S.P., Robinson, S.A., Surlyk, F., Piasecki, S., 2002. Terrestrial and marine mass extinction at the Triassic–Jurassic boundary synchronized with major carbon-cycle perturbation: a link to initiation of massive volcanism? Geology 30, 251–254.

Hesselbo, S.P., McRoberts, C.A., Pálfy, J., 2007. Triassic–Jurassic boundary events: problems, progress, possibilities. Palaeogeogr. Palaeoclimat. Palaeoecol. 244, 1–10.

Hillebrandt, A. von, Krystyn, L., 2009. On the oldest Jurassic ammonites of Europe (Northern Calcareous Alps, Austria) and their global significance. N. Jb. Geol. Paläont. Abh. 253, 163–195.

Hillebrandt, A. von, Krystyn, L., Kuerschner, W.M., 2007. A candidate GSSP for the base of the Jurassic in the Northern Calcareous Alps (Kuhjoch section, Karwendel Mountains, Tyrol, Austria). Int. Subcomm. Jurass. Stratigr. Newsl. 34, 2–20.

Hu, X., Wang, Y.L., Schmitt, R.A., 1988. Geochemistry of sediments on the Rio Grande Rise and the redox evolution of the south Atlantic Ocean. Geochim. Cosmochim. Acta 52, 201–207.
Kiessling, W., Aberhan, M., Brenneis, B., Wagner, P.J., 2007. Extinction trajectories of benthic organisms across the Triassic–Jurassic boundary. Palaeogeogr. Palaeoclimat. Palaeoecol. 244, 201–222.
Klein, E.M., 2003. Geochemistry of the igneous oceanic crust. In: Heinrich, D.H., Karl, K.T. (Eds.), Treatise on Geochemistry. Pergamon, Oxford, pp. 433–463.
Kozur, H.W., Weems, R.E., 2010. The biostratigraphic importance of conchostracans in the continental Triassic of the northern hemisphere. In: Lucas, S.G. (Ed.), The Triassic Timescale, 334. Geological Society of London Special Publication, pp. 315–417.
Krystyn, L., Böhm, F., Kürschner, W., Delecat, S., 2005. The Triassic–Jurassic boundary in the Northern Calcareous Alps. In: Pálfy, J., Ozsvárt, P. (Eds.), Program, Abstracts and Field Guide, 5th Field Workshop of IGCP 458 Project (Tata and Hallein), pp. A1–A14.
Kürschner, W.M., Bonis, N.R., Krystyn, L., 2007. Carbon-isotope stratigraphy and palynostratigraphy of the Triassic–Jurassic transition in the Tiefengraben section—Northern Calcareous Alps (Austria). Palaeogeogr. Palaeoclimat. Palaeoecol. 244, 257–280.
Linzer, H.-G., Ratschbacher, L., Frisch, W., 1995. Transpressional collision structures in the upper crust: the fold-thrust belt of the Northern Calcareous Alps. Tectonophysics 242, 41–61.
Marzoli, A., Renne, P.R., Piccirillo, E.M., Ernesto, M., Bellieni, G., De Min, A., 1999. Extensive 200-million-year-old continental flood basalts of the Central Atlantic Magmatic Province. Science 284, 616–618.
Marzoli, A., Bertrand, H., Knight, K.B., Cirilli, S., Buratti, N., Verati, C., Nomade, S., Renne, P.R., Youbi, N., Martini, R., Allenbach, K., Neuwerth, R., Rapaille, C., Zaninetti, L., Bellieni, G., 2004. Synchrony of the Central Atlantic magmatic province and the Triassic–Jurassic boundary climatic and biotic crisis. Geology 32, 973–976.
Marzoli, A., Jourdan, F., Puffer, J.H., Cuppone, T., Tanner, L.H., Weems, R.E., Bertrand, H., Cirilli, S., Bellieni, G., De Min, A., 2011. Timing and duration of the Central Atlantic magmatic province in the Newark and Culpeper basins, eastern U.S.A. Lithos 122, 175–188.
McElwain, J.C., Punyasena, S.W., 2007. Mass extinction events and the plant fossil record. Trends Ecol. Evol. 22, 548–557.
McElwain, J.C., Beerling, D.J., Woodward, F.I., 1999. Fossil plants and global warming at the Triassic–Jurassic Boundary. Science 285, 1386–1390.
McElwain, J.C., Popa, M.E., Hesselbo, S.P., Haworth, M., Surlyk, F., 2007. Macroecological responses of terrestrial vegetation to climatic and atmospheric change across the Triassic/Jurassic boundary in East Greenland. Paleobiology 33, 547–573.
McGhee, G.R., Sheehan, P.M., Bottjer, D.J., Droser, M.L., 2004. Ecological ranking of Phanerozoic biodiversity crises: ecological and taxonomic severities are decoupled. Palaeogeogr. Palaeoclimat. Palaeoecol. 211, 289–297.
McLennan, S.M., 1989. Rare earth elements in sedimentary rocks: influence of provenance and sedimentary processes. In: Lipin, B.R., McKay, G.A. (Eds.), Geochemistry and mineralogy of rare earth elements. Rev. Mineral. 21, 169–200.
McRoberts, C.A., Furrer, H., Jones, D.S., 1997. Palaeoenvironmental interpretation of a Triassic–Jurassic boundary section from Western Austria based on palaeoecological and geochemical data. Palaeogeogr. Palaeoclimat. Palaeoecol 136, 79–95.
Michalík, J., Biroň, A., Lintnerová, O., Götz, A.E., Ruckwied, K., 2010. Climate change at the Triassic/Jurassic boundary in the northwestern Tethyan realm, inferred from sections in the Tatra Mountains (Slovakia). Acta Geol. Pol. 60, 535–548.
Morante, R., Hallam, A., 1996. Organic carbon isotopic record across the Triassic–Jurassic boundary in Austria and its bearing on the cause of the mass extinction. Geology 24, 391–394.
Morbey, S.J., 1975. The palynostratigraphy of the Rhaetian stage, Upper Triassic, in the Kendelbachgraben, Austria. Palaeontographica, Abt. B 152, 1–75.
Myers, K.J., Wignall, P.B., 1987. Understanding Jurassic organic-rich mudrocks—new concepts using gamma-ray spectrometry and palaeoecology: examples from the Kimmeridge Clay of Dorset and the Jet rock of Yorkshire. In: Leggett, J.K., Zuffa, G.G. (Eds.), Marine Clastic Sedimentology. Graham and Trotman, London, pp. 172–189.
Nomade, S., Knight, K.B., Beutel, E., Renne, P.R., Verati, C., Feraud, G., Marzoli, A., Youbi, N., Bertrand, H., 2007. Chronology of the Central Atlantic Magmatic Province: implications for the Central Atlantic rifting processes and the Triassic–Jurassic biotic crisis. Palaeogeogr. Palaeoclimat. Palaeoecol 244, 326–344.
Olsen, P.E., Shubin, N.H., Anders, M.H., 1987. New Early Jurassic tetrapod assemblages constrain Triassic–Jurassic tetrapod extinction event. Science 237, 1025–1029.
Olsen, P.E., Kent, D.V., Sues, H.-D., Koeberl, C., Huber, H., Montanari, A., Rainforth, E.C., Fowell, S.J., Szajna, M.J., Hartline, B.W., 2002. Ascent of dinosaurs linked to an iridium anomaly at the Triassic–Jurassic boundary. Science 296, 1305–1307.
Olsen, P.E., Kent, D.V., Et-Touhami, M., Puffer, J., 2003. Cyclo-, magneto-, and biostratigraphic constraints on the duration of the CAMP event and its relationship to the Triassic–Jurassic boundary. In: Hames, W.E., McHone, J.G., Renne, P.R., Ruppel, C. (Eds), The Central Atlantic Magmatic Province: Insights from fragments of Pangea. Geophysical Monograph Series, vol. 136, pp. 7–32.
Pálfy, J., 2003. Volcanism of the Central Atlantic Magmatic Province as a potential driving force in the end-Triassic mass extinction. In: Hames, W.E., McHone, J.G., Renne, P.R., Ruppel, C. (Eds), The Central Atlantic Magmatic Province: Insights from fragments of Pangea. AGU Geophysical Monograph Series, vol. 136, pp. 255–267.
Pálfy, J., Mortensen, J.K., Carter, E.S., Smith, P.L., Friedman, R.M., Tipper, H.W., 2000. Timing the end-Triassic mass extinction: first on land, then in the sea? Geology 28, 39–42.
Pálfy, J., Demény, A., Haas, J., Hetényi, M., Orchard, M., Vető, I., 2001. Carbon isotope anomaly and other geochemical changes at the Triassic–Jurassic boundary from a marine section in Hungary. Geology 29, 1047–1050.
Raup, D.M., Sepkoski Jr., J.J., 1982. Mass extinctions in the marine fossil record. Science 215, 1501–1503.
Ruhl, M., Kuerschner, W.M., Krystyn, L., 2009. Triassic–Jurassic organic carbon isotope stratigraphy of key sections in the western Tethys realm (Austria). Earth Planet. Sci. Lett. 281, 169–187.
Schaller, M.F., Wright, J.D., Kent, D.V., 2011. Atmospheric pCO_2 perturbations associated with the Central Atlantic Magmatic Province. Science 331, 1404–1409.
Schaltegger, U., Guex, J., Bartolini, A., Schoene, B., Ovtcharova, M., 2008. Precise U-Pb age constraints for end-Triassic mass extinction, its correlation to volcanism and Hettangian post-extinction recovery. Earth Planet. Sci. Lett. 267, 266–275.
Schijf, J., DeBaar, H.J.W., 1995. Rare earth element exchange through the Bosporus: the Black Sea as a net source of REEs to the Mediterranean Sea. Geochim. Cosmochim. Acta 59, 3503–3509.
Schoene, B., Guex, J., Bartolini, A., Schaltegger, U., Blackburn, T.J., 2010. Correlating the end-Triassic mass extinction and flood basalt volcanism at the 100 ka level. Geology 38, 387–390.
Sepkoski, J.J., 1981. A factor analytic description of the Phanerozoic marine fossil record. Paleobiology 7, 36–53.
Sepkoski, J.J., 1993. Ten years in the library: new data confirm paleontological patterns. Paleobiology 19, 43–51.
Sholkovitz, E.R., Schneider, D.L., 1991. Cerium redox cycles and rare earth elements in the Sargasso Sea. Geochim. Cosmochim. Acta 55, 2737–2743.
Steinthorsdottir, M., Jeram, A.J., McElwain, J.C., 2011. Extremely elevated CO_2 concentrations at the Triassic/Jurassic boundary. Palaeogeogr. Palaeoclimat. Palaeoecol. 308, 418–432.
Suess, E., Mojsisovics, E., 1868. Studien über die Trias- und Jurabildungen in den östlichen Alpen. Die Gebirgsgruppe des Osterhornes. Jb. kais.kön. geol. Reichanst 18, 168–200.
van de Schootbrugge, B., Quan, T.M., Lindstrom, S., Puttmann, W., Heunisch, C., Pross, J., Fiebig, J., Petschick, R., Rohling, H.G., Richoz, S., Rosenthal, Y., Falkowski, P.G., 2009. Floral changes across the Triassic/Jurassic boundary linked to flood basalt volcanism. Nat. Geosci. 2, 589–594.
Velde, B., Meunier, A., 2008. The origin of clay minerals in soils and weathered rocks. Springer, Berlin, Heidelberg. Vine, J. D., Tourtelot, E. B., 1970. Geochemistry of black shale deposits—a summary report. Econ. Geol. 65: 253–272.
Wang, P., 2009. Global monsoon in a geological perspective. Chin. Sci. Bull. 54, 1113–1136.
Ward, P.D., Haggart, J.W., Carter, E.S., Wilbur, D., Tipper, H.W., Evans, T., 2001. Sudden productivity collapse associated with the Triassic–Jurassic boundary mass extinction. Science 292, 1148–1151.
Whiteside, J.H., Olsen, P.E., Kent, D.V., Fowell, S.J., Et-Touhami, M., 2007. Synchrony between the Central Atlantic magmatic province and the Triassic–Jurassic mass-extinction event? Palaeogeogr. Palaeoclimat. Palaeoecol 244, 345–367.
Wignall, P.B., Newton, R., 1998. Pyrite framboid diameter as a measure of oxygen deficiency in ancient mudrocks. Am. J. Sci. 298, 537–552.
Wignall, P.B., Newton, R., Brookfield, M.E., 2005. Pyrite framboid evidence for oxygen-poor deposition during the Permian–Triassic crisis in Kashmir. Palaeogeogr. Palaeoclimat. Palaeoecol 216, 183–188.
Wilkin, R.T., Barnes, H.L., Brantley, S.L., 1996. The size distribution of framboidal pyrite in modern sediments: an indicator of redox conditions. Geochim. Cosmochim. Acta 60, 3897–3912.
Zajzon, N., Kristály, F., Pálfy, J., Németh, T., 2012. Detailed clay mineralogy of the Triassic–Jurassic boundary section at Kendlbachgraben (Northern Calcareous Alps, Austria). Clay Miner 47, 177–189.